
Article:
Verhoosel, C.V., van Zwieten, G.J., van Rietbergen, B. et al. (1 more author) (2015) Image-based goal-oriented adaptive isogeometric analysis with application to the micro-mechanical modeling of trabecular bone. Computer Methods in Applied Mechanics and Engineering, 284. pp. 138-164. ISSN 0045-7825

https://doi.org/10.1016/j.cma.2014.07.009

Image-based goal-oriented adaptive isogeometric analysis with application to the micro-mechanical modeling of trabecular bone

C.V. Verhoosel[a,*], G. J. van Zwieten[a], B. van Rietbergen[b], R. de Borst[c]

[a] *Department of Mechanical Engineering, Eindhoven University of Technology, 5600 MB Eindhoven, The Netherlands*
[b] *Department of Biomedical Engineering, Eindhoven University of Technology, 5600 MB Eindhoven, The Netherlands*
[c] *School of Engineering, University of Glasgow, Glasgow G12 8LT, UK*

Abstract

Isogeometric analysis (IGA) of geometrically complex three-dimensional objects is possible when used in combination with the Finite Cell method (FCM). In this contribution we propose a computational methodology to automatically analyze the effective elastic properties of scan-based volumetric objects of arbitrary geometric and topological complexity. The first step is the reconstruction of a smooth geometry from scan-based voxel data using a B-spline level set function. The second step is a goal-oriented adaptive isogeometric linear elastic analysis. Elements are selected for refinement using dual-weighted residual shape function indicators, and hierarchical splines are employed to construct locally refined spline spaces. The proposed methodology is studied in detail for various numerical test cases, including the computation of the effective Young's modulus of a trabecular bone micro-structure reproduced from μCT-scan data.

Keywords: Isogeometric analysis, Finite cell method, Hierarchical splines, Goal-oriented error estimation and adaptivity, Image-based analysis, Trabecular bone micro-structures

*Corresponding author. Phone: +31 40 247 2382
Email addresses: c.v.verhoosel@tue.nl (C.V. Verhoosel), g.j.v.zwieten@tue.nl (G. J. van Zwieten), b.v.rietbergen@tue.nl (B. van Rietbergen), rene.deborst@glasgow.ac.uk (R. de Borst)

1. Introduction

Isogeometric analysis (IGA) was introduced by Hughes *et al.* in 2005 [1] as a novel analysis paradigm aiming at the unification of the fields of computer aided (geometric) design (CAD) and finite element analysis (FEA), see also [2]. The fundamental idea of IGA is to directly use the CAD parametrization of a geometric design for the purpose of analysis. Consequently, in contrast to the finite element method, no geometry clean-up or meshing operations are required. This rigorous elimination of the meshing step benefits the design-through-analysis process, especially for complex designs. Additionally, the spline basis functions inherited from CAD have various advantageous properties compared to the basis functions used in finite elements. The smoothness of higher-order spline basis functions is the most prominent of such advantageous properties. Due to its merits, isogeometric analysis has been applied in the context of both Galerkin-based and collocation-based (*e.g.* [3, 4]) analysis for a wide variety of applications, encompassing the domains of fluid dynamics, (non-linear) solid mechanics, and multi-physics modeling. Finite element data structures have been developed to facilitate the implementation of the isogeometric analysis paradigm in existing finite element codes, see *e.g.* [5–7].

Recently, isogeometric analysis has successfully been applied for the discretization of a variety of problems on geometrically and topologically complex volumetric domains by using it in conjunction with the finite cell method [8, 9]. In this method a trivariate tensor-product domain is created in which the complex domain of interest is immersed [10, 11]. The B-spline (or NURBS) basis functions required for the construction of trial and test spaces to be used in combination with a Galerkin problem are initially constructed over the structured domain, after which they are restricted to the domain of interest. Since an underlying structured mesh is available, local refinements can be obtained using hierarchical splines, see *e.g.* [12].

A particularly interesting application area of the finite cell method is the analysis of image-based (or scan-based) geometric models [13]. Since the finite cell method does not require a conforming mesh, cumbersome meshing operations can be circumvented. Instead, the image data is used on a sub-element level to trim the structured domain to the immersed domain of interest. The image-based finite cell method has been used for *e.g.* the analysis of metal foams [14], the validation of in vitro bone experiments [15], and trabecular bone micro-structures [11] (see [13] for an overview).

In this contribution we study the application of the isogeometric finite

cell method to the elastic analysis of trabecular bone specimens. Numerical analysis of trabecular bone plays an important role in efficacy studies of osteoporosis treatments. In the last few decades micro-scale finite element techniques have been proposed that use a voxel conversion technique to represent the bone micro-structure with brick elements (see *e.g.* [16–18]). Although such analyses can well predict bone stiffness in some clinical research studies, the disadvantages associated with such analyses prevent wider application. Most importantly, due to the non-smoothness of the geometric model, microscopic stresses cannot be represented accurately. Alternative finite element techniques, *e.g.* based on tetrahedral meshes (see *e.g.* [19–21]), have been developed to ameliorate the deficiencies of analyses using brick elements. However, due to the poor performance of linear tetrahedron elements, and the computational expenses of second order tetrahedrons, these are not commonly used. Based on its proven advantages, it is anticipated that isogeometric analysis can render accurate and reliable computational results for the elastic analysis of trabecular bone micro-structures. In this contribution we outline a computational methodology to automatically perform the elastic analysis of scan-based geometric models with a high degree of computational accuracy.

One of the novel contributions of this manuscript is the introduction and analysis of a B-spline-based approximation strategy for gray scale voxel data, which provides an implicit definition of the scan-based geometry with a smooth internal boundary. The second novelty of this work is the usage of goal-oriented adaptive analysis [22] in the context of the scan-based isogeometric finite cell method. This aspect of our work builds on the recent work in [23], where goal-oriented isogeometric analysis is considered in the context of tensor-product B-splines. The usage of adaptive methods is of paramount importance in the context of three-dimensional scan-based geometric models, since manual refinement operations are impractical. These operations involve both the aspect of identifying regions with high contributions to the error in the quantity of interest, and the actual refinement of the elements in these regions. In addition to these two main contributions, we outline various details of the finite cell method that are specific to our work. Most importantly, we employ and study a simplex-based tessellation of the elements that intersect the boundary of the physical domain.

The computational methodology proposed in this work is first studied for two-dimensional test cases, for which high accuracy reference solutions can be computed. This allows us to perform detailed convergence studies,

and to assess the quality of our error estimates. Subsequently we apply the methodology to the elastic analysis of a realistic data set obtained by a μCT-scan of a trabecular bone micro-structure. Our terminology is tailored to the three-dimensional setting. The words "pixel" and "voxel" are for example used synonymously in the two-dimensional setting. We will also use the terms "volume" and "surface area" in the two-dimensional case, referring to areas and edge lengths, respectively.

In Section 2 we will discuss the scan-based definition of the computational domain, and study the main properties of the proposed B-spline smoothing operation. In Section 3 the linear elasticity problem is introduced along with the isogeometric discretization and the error estimation and adaptivity framework. In Section 4 we discuss various computational aspects of our work, after which three numerical test cases are studied in detail in Section 5. Our conclusions are summarized in Section 6.

2. Scan-based geometry definition

In this section we introduce the scan-based geometry definition. As an example we consider the two-dimensional bone geometry depicted in Figure 1, which has been created in a vector graphics editor. The consideration of this artificial specimen is particularly useful since it permits us to compare the geometry reproduced from the scan data with the real geometry. Simulated scan data for this geometry are constructed by computing the bone volume fractions per pixel, and performing a shift such that the domain boundary is characterized by a zero value. As we will see later, this geometry can be considered as representative for the geometry of real trabecular bone specimens. In particular, it reflects the topological complexity of real bone scan specimens in the sense that it contains holes and disconnected parts.

2.1. Spline-based level set geometry

The n_d-dimensional scan domain $\Omega_{\text{scan}} = \bigotimes_{d=1}^{n_d} [0, L_d] \subset \mathbb{R}^{n_d}$ with boundary $\partial\Omega_{\text{scan}}$ is partitioned by a set of voxels $\Omega^e_{\text{vox}} = \bigotimes_{d=1}^{n_d} ((\mathcal{I}(e)_d - 1)\Delta_d, \mathcal{I}(e)_d\Delta_d)$ with Δ_d the voxel size in direction d and $\mathcal{I}$ a function that maps an integer voxel index $e \in \{1, 2, \ldots, m_{\text{vox}}\}$ to the corresponding n_d-dimensional voxel indices (see Figure 1). The voxel gray scale function $g : \Omega_{\text{scan}} \to \mathbb{R}$ is defined

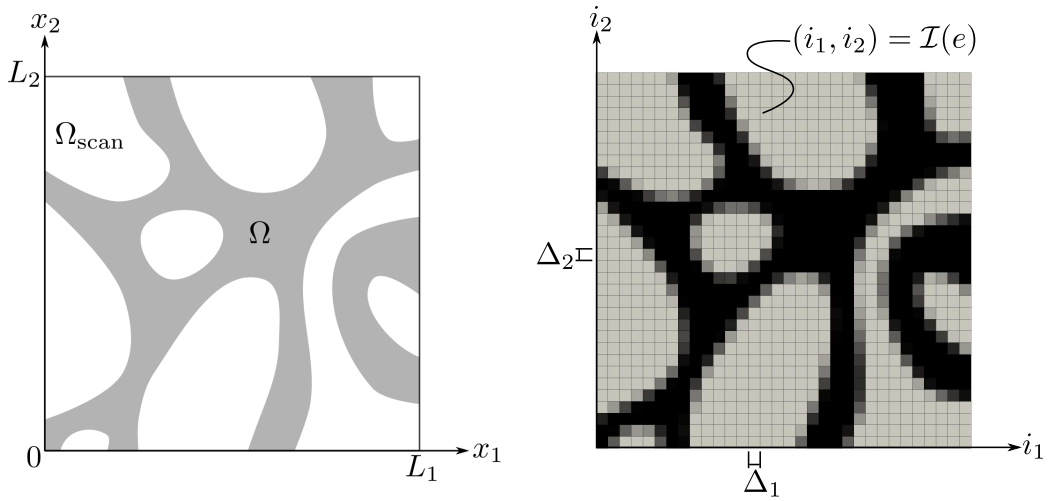

(a) (b)

Figure 1: (a) Two-dimensional bone geometry, Ω, inside a scan domain Ω_{scan}. (b) Virtual gray scale scan data (32×32 pixels) reproduced from the geometry in (a).

as

$$g(\boldsymbol{x}) = \begin{cases} c_1 & \boldsymbol{x} \in \Omega^1_{\text{vox}} \\ c_2 & \boldsymbol{x} \in \Omega^2_{\text{vox}} \\ \vdots & \vdots \\ c_{m_{\text{vox}}} & \boldsymbol{x} \in \Omega^{m_{\text{vox}}}_{\text{vox}} \end{cases} \tag{1}$$

with $\boldsymbol{c} \in \mathbb{R}^{m_{\text{vox}}}$ the gray scale values in the voxels $\{\Omega^e_{\text{vox}}\}_{e=1}^{m_{\text{vox}}}$. Note that for arbitrary data the function g is discontinuous. Moreover, often the gray scale values $\boldsymbol{c}$ are integer values ranging from *e.g.* 0 to 255.

A physical domain $\Omega \subseteq \Omega_{\text{scan}}$ can be extracted from the gray scale function directly by thresholding the voxels to yield $\Omega = \{\boldsymbol{x} \in \Omega_{\text{scan}} \mid g(\boldsymbol{x}) > g_{\text{crit}}\}$, for suitable threshold g_{crit}. The internal boundary of the resulting domain, $\mathcal{S} = \partial\Omega \backslash \partial\Omega_{\text{scan}}$, is non-smooth, which can significantly affect the approximation properties of discretization strategies. In order to optimally benefit from the smoothness properties of the isogeometric discretization used in this work, we therefore employ a smooth reconstruction of the geometry based on the original gray scale data.

In order to have an r-times continuously differentiable internal surface $\mathcal{S}$, a level set function $f \in C^r(\Omega_{\text{scan}})$ is required [24]. To obtain a smooth domain, a smooth ($r \geq 1$) level set function is therefore required. Here we

employ a smooth approximation of the exact geometry by the spline level set function

$$f(\boldsymbol{x}) = \sum_{i=1}^{n} N_{i,p}(\boldsymbol{x}) a_i, \tag{2}$$

with $\boldsymbol{a} \in \mathbb{R}^n$ the level set coefficients. The physical domain Ω, with smooth internal boundary $\mathcal{S}$, then follows as $\Omega = \{\boldsymbol{x} \in \Omega_{\text{scan}} \mid f(\boldsymbol{x}) > f_{\text{crit}}\}$ with f_{crit} the threshold value for the smoothed level set function f. In this work we use the same threshold level for the voxel data and the smooth level set, *i.e.* $f_{\text{crit}} = g_{\text{crit}}$.

The n basis functions $\{N_{i,p} : \Omega_{\text{scan}} \to \mathbb{R}\}_{i=1}^{n}$ are defined as the tensor product functions of the univariate open B-splines generated over the knot vectors $\Xi_d = [0, \ldots, 0, \Delta_d, 2\Delta_d, \ldots, L_d, \ldots, L_d]$ for $d = 1, \ldots, n_d$, where the first and last knot values are repeated $p+1$ times, see *e.g.* [25, 26]. Using this definition, the level set function f is $p-1$ times continuously differentiable, and hence a smooth surface $\mathcal{S}$ is obtained for $p \geq 2$.

A smooth approximation of the gray scale data g is constructed by computing the level set coefficients by

$$a_i = \frac{\int\limits_{\Omega_{\text{scan}}} N_{i,p}(\boldsymbol{x}) g(\boldsymbol{x})\, d\boldsymbol{x}}{\int\limits_{\Omega_{\text{scan}}} N_{i,p}(\boldsymbol{x})\, d\boldsymbol{x}} = \frac{1}{V_{N_{i,p}}} \int\limits_{\Omega_{\text{scan}}} N_{i,p}(\boldsymbol{x}) g(\boldsymbol{x})\, d\boldsymbol{x} \qquad i = 1, \ldots n, \tag{3}$$

which upon substitution in equation (2) yields the B-spline level set function f. This convolution-based strategy is preferred over an L^2-projection or collocation strategy because of its reconstruction properties, which we will study in detail in Section 2.2: *i)* the gray scale intensity of the voxel data is preserved; *ii)* the reconstructed data is bounded by the scan data; *iii)* the spectral filtering properties are favorable. An important additional advantage of this convolution-based reconstruction strategy is its computational efficiency resulting from the fact that it is not required to solve a linear system of equations, this in contrast to *e.g.* an L^2-projection.

In Figure 2b the quadratic B-spline level set function generated for the 32×32 pixel data structure in Figure 2a is shown. In Figure 3 the dependence of the geometry approximation on the resolution of the original pixel data is illustrated by a comparison of the geometry obtained on both a 16×16 pixel structure and the 32×32 pixel data. Evidently, the quality of the

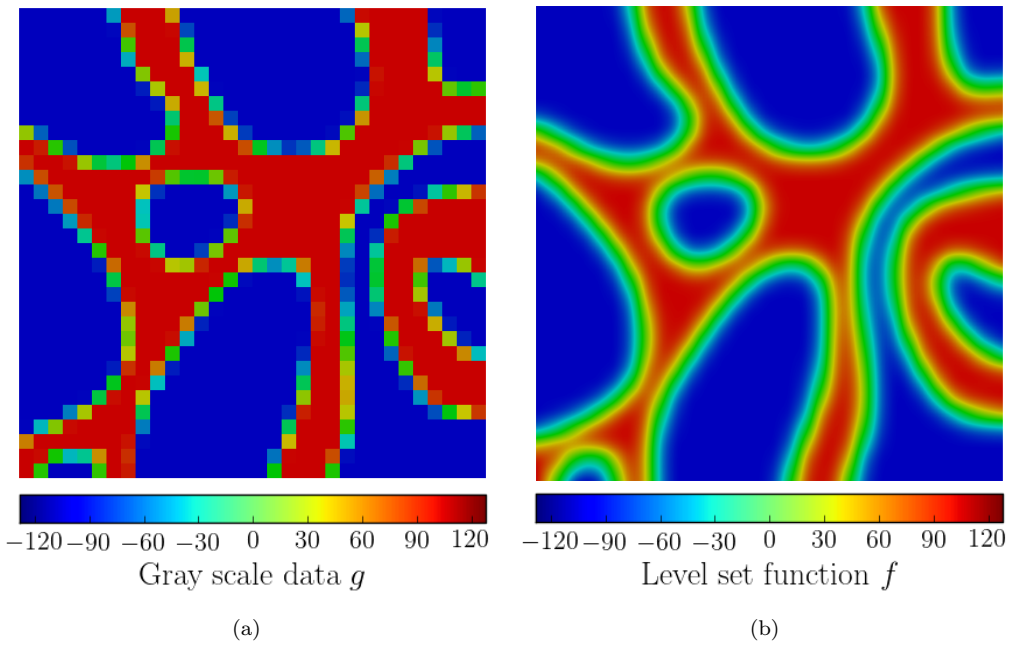

(a) (b)

Figure 2: (a) Gray scale data consisting of 32×32 pixels, and (b) its second-order B-spline level set function approximation.

approximation strongly depends on the resolution of the pixel data. From Figure 3 it is observed that even for low resolution data the characteristic features of the real geometry, such as the cavity and the gap between the two disconnected parts, are preserved in the smoothing operation. For the present case the geometry generated from the 32×32 pixel data can hardly be distinguished from the exact geometry.

2.2. Properties of the spline-based level set function

2.2.1. Conservation of gray scale intensity

The smooth spline approximation (2) conserves the average gray scale intensity of the pixel data:

$$\frac{1}{V_{\text{scan}}} \int_{\Omega_{\text{scan}}} f(\boldsymbol{x})\, d\boldsymbol{x} = \frac{1}{V_{\text{scan}}} \int_{\Omega_{\text{scan}}} g(\boldsymbol{x})\, d\boldsymbol{x} = \frac{1}{m_{\text{vox}}} \sum_{e=1}^{m_{\text{vox}}} c_e. \tag{4}$$

Note that without this property there is no apparent relation between the threshold value for smooth level set reconstruction (f_{crit}) and that of the original data (g_{crit}).

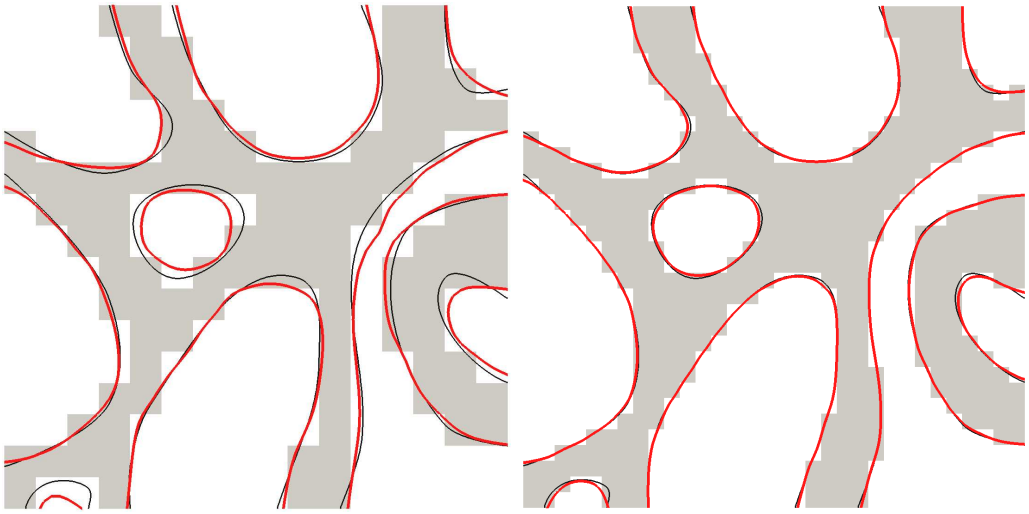

(a) 16×16 pixels (b) 32×32 pixels

Figure 3: The second-order B-spline geometry reconstruction with $f_{\text{crit}} = 0$ (red) based on a pixel data set (gray) consisting of (a) 16×16 and (b) 32×32 pixels. The contour of the exact geometry is shown in black for comparison.

This property can be verified by rewriting equation (3) as

$$\int_{\Omega_{\text{scan}}} N_{i,p}(\boldsymbol{x}) a_i \, d\boldsymbol{x} = \int_{\Omega_{\text{scan}}} N_{i,p}(\boldsymbol{x}) g(\boldsymbol{x}) \, d\boldsymbol{x} \qquad i = 1, \ldots, n, \tag{5}$$

summarizing it over the index i, and making use of the B-spline level set definition (2) and the partition of unity property of the spline basis.

2.2.2. Local boundedness

On every (voxel) subdomain, Ω^e_{vox}, the level set function is bounded by the minimum and maximum values of the pixel data over all voxels covered by the B-spline functions with support over this subdomain,

$$\min_{\boldsymbol{x} \in \Omega^e_{\text{supp}}} \left(g(\boldsymbol{x}) \right) \leq f(\boldsymbol{x}) \leq \max_{\boldsymbol{x} \in \Omega^e_{\text{supp}}} \left(g(\boldsymbol{x}) \right) \qquad \forall \boldsymbol{x} \in \Omega^e_{\text{vox}}, \tag{6}$$

with $\Omega^e_{\text{supp}} = \cup_{i \in \mathcal{I}_e} \operatorname{supp}\left(N_{i,p}\right)$ and $\mathcal{I}_e = \{i \mid N_{i,p}|_{\Omega^e_{\text{vox}}} \neq 0\}$. These bounds can be verified by combining the boundedness of the level set function by the control point level set values, $\{a_i\}_{i \in \mathcal{I}_e}$,

$$\min_{i \in \mathcal{I}_e}(a_i) \leq f|_{\Omega^e_{\text{vox}}} \left(= \sum_{i \in \mathcal{I}_e} N_{i,p} a_i \right) \leq \max_{i \in \mathcal{I}_e}(a_i) \tag{7}$$

and the fact that, following directly from equation (3), the control point level set values are bounded by the gray scale data:

$$\min_{\boldsymbol{x}\in\mathrm{supp}\,(N_{i,p})}\left(g(\boldsymbol{x})\right) \leq a_i \leq \max_{\boldsymbol{x}\in\mathrm{supp}\,(N_{i,p})}\left(g(\boldsymbol{x})\right) \qquad i=1,\ldots,n. \tag{8}$$

Note that in (7) use is made of the non-negativity and partition of unity property of the B-spline basis functions.

The local boundedness of the level set function f implies global boundedness by the global minimum and maximum gray scale values. The existence of the bounds precludes overshoots and undershoots, which indicates that no spurious oscillations are created by the smoothing procedure. It is noted that such oscillations can occur when *e.g.* an L^2-projection is used to determine the level set values.

2.2.3. The approximation kernel

To study the smoothing behavior of the B-spline level set approximation f we substitute the control point gray scale values, equation (3), in the B-spline function (2) to obtain

$$f(\boldsymbol{x}) = \int_{\Omega_{\mathrm{scan}}} \left[\sum_{i=1}^{n} \frac{N_{i,p}(\boldsymbol{x})N_{i,p}(\boldsymbol{y})}{V_{N_{i,p}}}\right] g(\boldsymbol{y})\,d\boldsymbol{y}, \tag{9}$$

which shows that $f(\boldsymbol{x})$ is an integral transform of the data $g(\boldsymbol{x})$ with the kernel

$$K(\boldsymbol{x},\boldsymbol{y}) = \sum_{i=1}^{n} \frac{N_{i,p}(\boldsymbol{x})N_{i,p}(\boldsymbol{y})}{V_{N_{i,p}}}. \tag{10}$$

To analyze the integral transform (9) we consider a univariate spline basis of order p defined over the uniform knot vector $\Xi = [\ldots,-2\Delta,-\Delta,0,\Delta,2\Delta,\ldots]$ if p is odd or $\Xi = [\ldots,-\frac{3}{2}\Delta,-\frac{1}{2}\Delta,\frac{1}{2}\Delta,\frac{3}{2}\Delta\ldots]$ if p is even (with pixel size Δ). For our analysis we approximate the B-spline basis functions, $N_{i,p}(\xi)$, constructed over these knot vectors by

$$N_{i,p}(\xi) \approx \tilde{N}_{i,p}(\xi) = \sqrt{\frac{6}{\pi(p+1)}}\left(e^{-\frac{6\left(i+\frac{\xi}{\Delta}\right)^2}{p+1}}\right), \tag{11}$$

for which it has been proven [27] that $\lim_{p\to\infty} \tilde{N}_{i,p} = N_{i,p}$ (see Figure 4). Note that $i = \ldots,-2,-1,0,1,2,\ldots$ and that the basis function $N_{0,p}$ is centered

at $\xi = 0$. Substitution of this approximation into the kernel (10) yields

$$K(x,y) \approx \sqrt{\frac{3}{\pi\Delta^2(p+1)}}\,\vartheta_3\left(\frac{\pi(x+y)}{2\Delta}, e^{-\frac{1}{12}(1+p)\pi^2}\right) e^{-\frac{3(y-x)^2}{\Delta^2(1+p)}} \tag{12}$$

with ϑ_3 the third Jacobi theta function [28]. For all considered spline orders, the second argument of this theta function is much smaller than one, which renders $\vartheta_3 \approx 1$ to be a reasonable approximation. Substitution of this approximation yields the convolution kernel

$$K(x,y) \approx \sqrt{\frac{3}{\pi\Delta^2(p+1)}} e^{-\frac{3(y-x)^2}{\Delta^2(1+p)}} = \tilde{K}(y-x). \tag{13}$$

In Figure 5 we show the original kernel (10) and the convolution approximation (13) for the case of $p = 3$. As observed, the primary characteristics of the original transformation kernel are preserved in the convolution approximation.

The convolution kernel (13) is of the same form as those commonly used in image processing techniques [29] and acts as a Gaussian filter [30]. In Figure 6 this kernel is shown for various orders of the spline basis. For comparison, the ideal (Sinc) filter is also depicted. This ideal filter preserves all frequencies in the pixel data and completely filters out all higher-order frequencies. Upon increasing the order of the B-spline approximation, the smoothing operation behaves more as a low-pass filter, in which high frequencies are filtered out. In Figure 7 we show the potential effect of this smoothing operation when the resolution of the original data is insufficient. High frequency features, such as the gap between the two disconnected parts, can be affected by the smoothing operation. The robust use of the smoothing procedure relies on the assumption that the resolution of the scan data is sufficient to distinguish the main features of the underlying geometry.

3. Goal-adaptive isogeometric analysis

3.1. Problem definition

In this contribution the material in the physical domain, with deformation $\boldsymbol{u} : \Omega \to \mathbb{R}^{n_d}$, is modeled by means of linear elasticity. The internal surface $\mathcal{S}$ is assumed to be traction-free, resulting in homogeneous Neumann

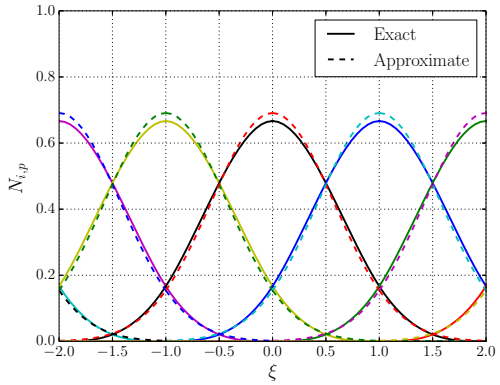

Figure 4: Cubic ($p = 3$) B-spline functions (solid lines) and their approximation by equation (11) (dashed lines).

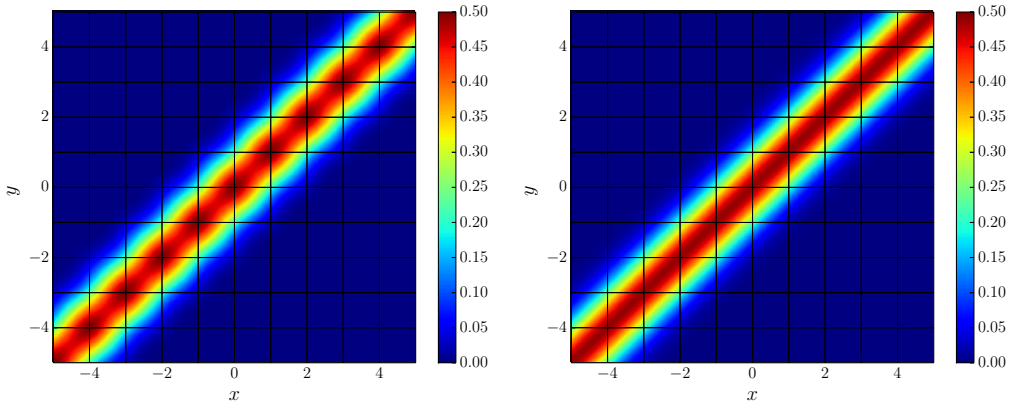

(a) B-spline kernel

(b) Convolution kernel

Figure 5: (a) The integral transformation kernel (10), and (b) the approximate convolution kernel (13) for $\Delta = 1$ and $p = 3$.

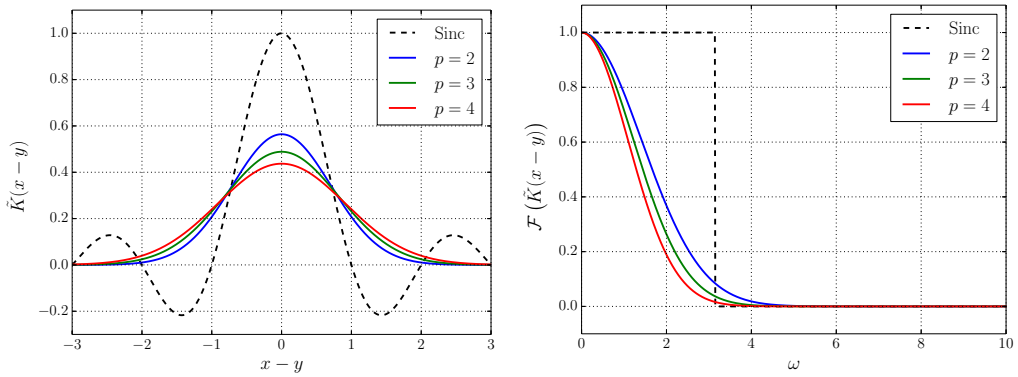

(a) (b)

Figure 6: The convolution kernel (13) in (a) the spatial and (b) the frequency domain for $\Delta = 1$ and various orders p.

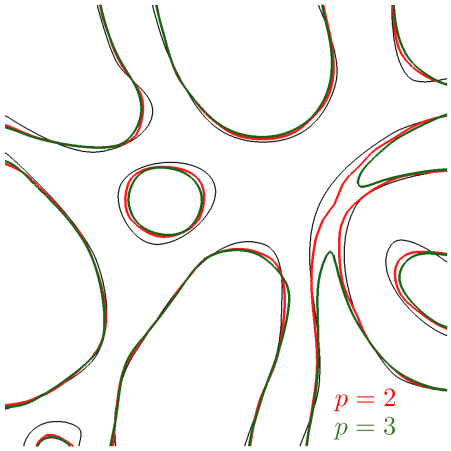

Figure 7: The influence of the order of the B-spline on the approximation of the geometry. The results are based on a data set with 16×16 pixels. The contour of the exact geometry is shown in black for comparison.

boundary conditions. On the scan domain boundaries, $\partial\Omega \cap \partial\Omega_{\text{scan}}$, the normal displacement is prescribed by the (partially homogeneous) Dirichlet data $g_n : \partial\Omega \cap \partial\Omega_{\text{scan}} \to \mathbb{R}$, while the tangential tractions are assumed to vanish. The strong form problem is then given by

$$(S) \quad \begin{cases} \operatorname{div}(\boldsymbol{\sigma}) = \mathbf{0} & \text{in } \Omega \quad (14) \\ \boldsymbol{\sigma} = 2\mu\boldsymbol{\varepsilon} + \lambda \operatorname{tr}(\boldsymbol{\varepsilon})\boldsymbol{I} & \text{in } \Omega \quad (15) \\ u_n = \boldsymbol{u} \cdot \boldsymbol{n} = g_n & \text{on } \partial\Omega \cap \partial\Omega_{\text{scan}} \quad (16) \end{cases}$$

where $\boldsymbol{\varepsilon} = \nabla^s \boldsymbol{u}$ is the infinitesimal strain tensor and μ and λ are the Lamé parameters for Hooke's law (15).

To derive the weak form primal problem (P) corresponding to the strong form (S) we define the test space $\mathcal{V}_0 = \{\boldsymbol{u} \in H^1(\Omega) \mid u_n = 0 \text{ on } \partial\Omega \cap \partial\Omega_{\text{scan}}\}$ along with a lift function $\boldsymbol{q} \in H^1(\Omega)$ that satisfies the Dirichlet boundary conditions. Defining the trial space as $\mathcal{V} = \{\boldsymbol{v} + \boldsymbol{q} \mid \boldsymbol{v} \in \mathcal{V}_0\}$ then yields the weak form primal problem:

$$(P) \quad \begin{cases} \text{Find } \boldsymbol{u} \in \mathcal{V} \text{ such that:} \\ \quad \mathcal{B}(\boldsymbol{u}, \boldsymbol{w}) = \mathcal{F}(\boldsymbol{w}) \qquad \forall \boldsymbol{w} \in \mathcal{V}_0\,, \end{cases} \quad (17)$$

where the bilinear functional $\mathcal{B}$ and linear functional $\mathcal{F}$ are given by

$$\mathcal{B}(\boldsymbol{u}, \boldsymbol{w}) = \int_\Omega \boldsymbol{\sigma}(\boldsymbol{u}) : \nabla^s \boldsymbol{w}\, d\boldsymbol{x} \qquad \mathcal{F}(\boldsymbol{w}) = 0. \quad (18)$$

3.2. Hierarchical spline discretization

To discretize the primal problem (17) we use the finite cell method in combination with hierarchical B-splines [9]. We will here briefly discuss the most important aspects of the employed spline discretization. For details the reader is referred to *e.g.* [12].

Using the tensor-product structure of the n_d-dimensional scan domain, Ω_{scan}, we generate a sequence of R nested n_d-variate uniform B-spline bases, $\left\{\mathcal{S}_p^r\right\}_{r=0}^{R-1}$, of order p. The B-spline functions $\mathcal{S}_p^r \ni S : \Omega_{\text{scan}} \to \mathbb{R}$ are constructed over the knot vectors Ξ_d^r with $d = 1, \ldots, n_d$. These knot vectors are defined as $\Xi_d^r = \{0, \ldots, 0, h_d^r, 2h_d^r, \ldots, L_d - h_d^r, L_d, \ldots, L_d\}$, where $h_d^r = 2^{-r} h_d^0$ with $h_d^0 = L_d / m_d^0$ the knot spacing for the coarsest spline Bézier mesh, $\mathbb{B}^0$, with m_d^0 elements in direction d. The first and last knot values are repeated $p+1$ times in each direction to create an open spline basis. The interior knots

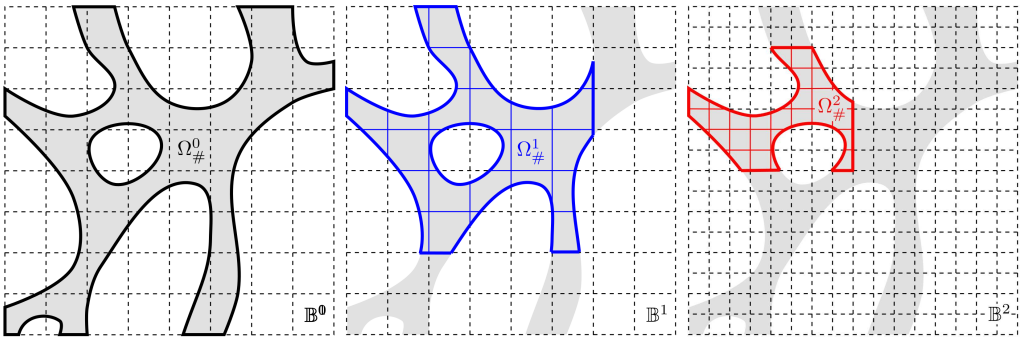

(a) Level 0 (b) Level 1 (c) Level 2

Figure 8: Schematic representation of the hierarchical spline levels.

are not repeated, such that the B-spline basis functions are C^{p-1}-continuous. Note that using this construction the parameter domain and the physical scan domain coincide.

We define the B-spline basis at level r as

$$\mathcal{N}_p^r = \left\{ N \in \mathcal{S}_p^r \mid \mathrm{supp}_\Omega\left(N\right) \neq \emptyset \right\}, \tag{19}$$

where $\mathrm{supp}_\Omega\left(N\right) = \{\boldsymbol{x} \in \Omega \mid N(\boldsymbol{x}) \neq 0\}$. By element refinement we then construct a sequence of nested subdomains, $\Omega^R_\# \subseteq \ldots \subseteq \Omega^1_\# \subseteq \Omega^0_\#$ (see Figure 8), with $\Omega^0_\# = \Omega$ and $\Omega^R_\# = \emptyset$. Using the sequence of B-spline bases, $\{\mathcal{N}_p^r\}_{r=0}^{R-1}$, we define an hierarchical spline basis $\mathcal{H}_p \ni N : \Omega \to \mathbb{R}$ as

$$\mathcal{H}_p = \bigcup_{r=0}^{R-1} \left\{ N \in \mathcal{N}_p^r \mid \mathrm{supp}_\Omega\left(N\right) \subseteq \Omega^r_\# \wedge \mathrm{supp}_\Omega\left(N\right) \nsubseteq \Omega^{r+1}_\# \right\}, \tag{20}$$

see *e.g.* [12, 23] for details, including a proof of global linear independence of $\mathcal{H}_p$.

Using the hierarchical basis (20) we can now create the finite dimensional approximation space for the primal problem (17) as

$$\mathcal{V}_0^h = \mathrm{span}\left(\{\boldsymbol{N} \mid \boldsymbol{N} \in \boldsymbol{\mathcal{H}}_p, N_n = 0 \text{ on } \partial\Omega \cap \partial\Omega_{\text{scan}}\}\right) \subset \mathcal{V}_0, \tag{21}$$

with $\boldsymbol{\mathcal{H}}_p$ the vector-valued version of $\mathcal{H}_p$.

In order to construct and integrate the basis functions numerically, we define the Bézier mesh for $\mathcal{V}_0^h$ as

$$\mathbb{B} = \mathbb{K}^0 \cup \left[\bigcup_{r=1}^{R-1} \left\{ K \in \mathbb{K}^r \mid K \nsubseteq \cup\mathbb{K}^{r-1} \right\} \right], \tag{22}$$

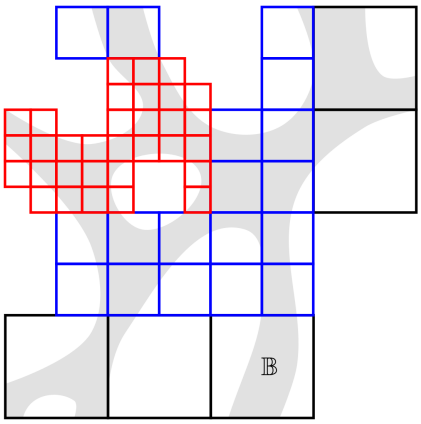

Figure 9: The hierarchical Bézier mesh $\mathbb{B}$ corresponding to the three levels shown in Figure 8.

with

$$\mathbb{K}^r = \left\{ K \in \mathbb{B}^r \mid K \cap \Omega \neq \emptyset \wedge K \cap \Omega_{\#}^{r+1} = \emptyset \right\}. \tag{23}$$

The Bézier mesh for the three levels of refinement introduced in Figure 8 is shown in Figure 9.

3.3. A-posteriori error estimation and adaptivity

In this contribution we aim at obtaining an optimal discretization for the computation of effective elastic properties. In the abstract setting considered here, an elastic property is expressed as a linear functional, $\mathcal{Q}(\boldsymbol{u})$, of the solution to the primal problem (17). By defining the dual problem

$$(D) \quad \begin{cases} \text{Find } \boldsymbol{z} \in \mathcal{V}_0 \text{ such that:} \\ \quad \mathcal{B}(\boldsymbol{w}, \boldsymbol{z}) = \mathcal{Q}(\boldsymbol{w}) \qquad \forall \boldsymbol{w} \in \mathcal{V}_0 \,, \end{cases} \tag{24}$$

the error in the quantity of interest can be computed as

$$\begin{aligned} \mathcal{E} &= \mathcal{Q}(\boldsymbol{u}) - \mathcal{Q}(\boldsymbol{u}^h) = \mathcal{Q}(\boldsymbol{v}) - \mathcal{Q}(\boldsymbol{v}^h) \\ &= \mathcal{B}(\boldsymbol{v}, \boldsymbol{z}) - \mathcal{B}(\boldsymbol{v}^h, \boldsymbol{z}) = \mathcal{B}(\boldsymbol{u}, \boldsymbol{z}) - \mathcal{B}(\boldsymbol{u}^h, \boldsymbol{z}) \\ &= \mathcal{F}(\boldsymbol{z}) - \mathcal{B}(\boldsymbol{u}^h, \boldsymbol{z}) = \mathcal{R}^h(\boldsymbol{z} - \boldsymbol{\psi}^h) \qquad \forall \boldsymbol{\psi}^h \in \mathcal{V}_0^h \end{aligned} \tag{25}$$

where use is made of Galerkin orthogonality in the final step and $\mathcal{R}^h(\boldsymbol{z})$ is referred to as the dual-weighted residual. In this contribution we estimate

the error by approximating the dual problem solution on a mesh which is obtained by a single uniform refinement of the primal problem mesh,

$$\text{Est} = \mathcal{R}^h(\boldsymbol{z}^{h/2} - \boldsymbol{\psi}^h), \tag{26}$$

and in order to obtain a sharp error estimate we take $\boldsymbol{\psi}^h$ as the L^2-projection of $\boldsymbol{z}^{h/2}$ on the primal problem space $\mathcal{V}_0^h$. We note that error estimators for isogeometric analysis based on the computation of a dual solution on an h-refined mesh have also been studied in [31]. Evidently, in terms of computational effort, the determination of the dual problem solution on a uniformly refined mesh is a relatively expensive operation, particularly in three-dimensional simulations. In fact, the computational overhead related to the adaptivity procedure is mainly comprised of this dual solution computation.

Using the functionals (18), the error estimate (26) is expressed as

$$\text{Est} = \int_\Omega -\boldsymbol{\sigma}(\boldsymbol{u}^h) : \nabla^s(\boldsymbol{z}^{h/2} - \boldsymbol{\psi}^h)\, d\boldsymbol{x}, \tag{27}$$

the integrand of which is referred to as the dual-weighted residual density. To use this error estimate for marking regions of refinement, we exploit the property of the hierarchical B-spline basis introduced in Section 3.2 that there exists a vector $\boldsymbol{\alpha}$ such that $\sum_{i=1}^n \alpha_i N_{i,p} = 1$. Using this property we obtain

$$\text{Est} = \sum_{i=1}^n -\alpha_i \int_\Omega N_{i,p}\boldsymbol{\sigma}(\boldsymbol{u}^h) : \nabla^s(\boldsymbol{z}^{h/2} - \boldsymbol{\psi}^h)\, d\boldsymbol{x} = \sum_{i=1}^n e_i, \tag{28}$$

where e_i is the error contribution of basis function $N_{i,p}$. Herein, we mark a fixed fraction, $\eta \in (0, 1]$, of the basis functions with the largest absolute error estimate contribution for refinement in each step. Subsequently, all elements in the support of the marked basis functions are refined to obtain the refined mesh on which the hierarchical spline basis can be constructed. Note that, following from the definition of the hierarchical space (20), this marking strategy always leads to refinement.

4. Computational aspects

In this section we discuss three important computational aspects of the isogeometric finite cell method used in this work: i) The numerical evaluation of integrals over trimmed elements; ii) The removal of basis functions to improve system conditioning; iii) The removal of geometric features that do not contribute to the quantity of interest.

4.1. Numerical integration of trimmed elements

An essential aspect of the finite cell method is the generation of a multi-level integration scheme for trimmed elements by recursive bisectioning (*e.g.* [8]). The integration point generation procedure used in this work is schematically shown in Figure 10. We define $\varrho_{\max}$ to be the maximum allowable number of bisections, *i.e.* no bisections are made if $\varrho_{\max} = 0$. Given a ϱ-times bisected integration cell, the decision on whether to perform a further bisection is based on the evaluation of the level set function in the $(2^{\varrho_{\max}-\varrho}+1)^{n_d}$ finest-level vertex locations. When all vertex values are positive, the cell is consolidated, while it is removed when all vertex values are negative. In the case of vertex values of both positive and negative sign, the integration cell is bisected if $\varrho < \varrho_{\max}$. On the finest level of integration, $\varrho = \varrho_{\max}$, we close this recursive procedure by a tessellation. Exact quadrature rules for higher-order polynomials are available for all integration cells, including the simplices generated by the tessellation.

The use of a tessellation on the finest level of integration contrasts the more common use of Gauss quadrature rules. Using a tessellation offers advantages in terms of integral approximation properties that – at least from the vantage point of the work presented in this manuscript – outweigh the additional computational effort involved in the tessellation procedure. An additional advantage of the tessellation-based integration scheme is that a boundary parametrization is directly obtained. Although this is not an exploited advantage in this work, this parametrization is of value when imposing non-homogeneous Neumann boundary conditions or weakly imposing Dirichlet boundary conditions over the trimmed boundary.

4.1.1. Tessellation procedure

On the finest level of integration a Delaunay tessellation is constructed. The set of points on which this tessellation is based consists of the integration cell vertices with non-negative level set values (indicated with plus-squares in Figure 10) and on the approximate level set function roots along the integration cell ribbons (indicated with zero-diamonds). These level set roots are computed based on a linear interpolation of the level set function along a ribbon. Note that although the employed level set is generally not a piecewise linear function, upon appropriate selection of $\varrho_{\max}$ a linear approximation of this function over the finest level cell ribbons is justified.

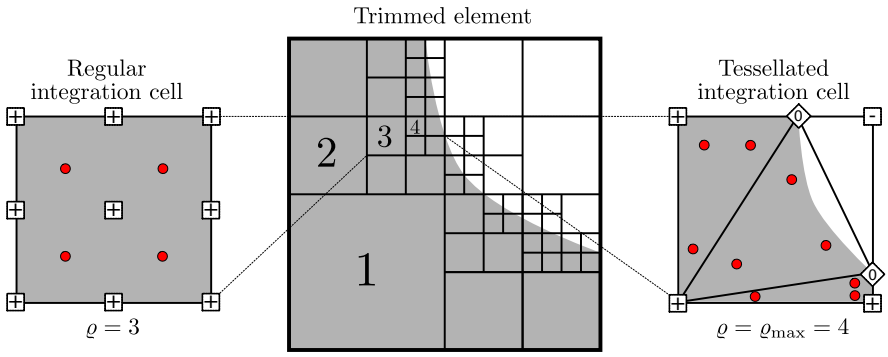

Figure 10: Schematic representation of the multi-level integration scheme used for trimmed elements. In this example the maximum number of cell bisections is taken as $\varrho_{\max} = 4$.

4.1.2. Approximation properties of simplex-based quadrature schemes

To analyze the approximation behavior of the simplex scheme we consider the finest level integration cell Ω^e_{int} with ribbon lengths $h_{\text{int}} = h^e/2^{\varrho_{\max}}$ as shown in Figure 11. Assuming, for the two-dimensional case, a domain boundary with constant radius of curvature R, the area integration error in this cell is equal to $e_{\text{int}} = \frac{h^3_{\text{edge}}}{12R}$, with h_{edge} the length of the interior boundary edge of the triangulation. Since $h_{\text{edge}} = O(h_{\text{int}})$ and the number of triangulated finest level cells scales with $O(h^{-1}_{\text{edge}}) = O(h^{-1}_{\text{int}})$ – the number of triangulated finest level cells times the average h_{edge} over these cells is of $O(1)$ – the total integration error over a two-dimensional trimmed element is $O(h^{-1}_{\text{int}}) \cdot O(h^3_{\text{int}}) = O(h^2_{\text{int}})$. This convergence rate extends to the three-dimensional case, $n_d = 3$, for which the volume integration error per finest level cell is $e_{\text{int}} = O(h^{n_d+1}_{\text{int}})$ and the total trimmed element integration error remains $O(h^{1-n_d}_{\text{int}}) \cdot O(h^{n_d+1}_{\text{int}}) = O(h^2_{\text{int}})$.

In Figure 12a we present the error convergence results for the integration of the volume of a sphere of radius R intersecting a unit square. Note that the above-mentioned order of convergence is recovered for the simplex scheme. For comparison the integration error is also shown for uniform and Gauss schemes. For these schemes it is observed that the convergence is not asymptotic for the cell sizes considered. This behavior can be explained by the fact that the volume integration error for these schemes is comprised of integration points overestimating the volume and integration points underestimating the volume (see Figure 11), which can cancel out. Under the assumption of sufficiently refined integration cells, the simplex scheme does

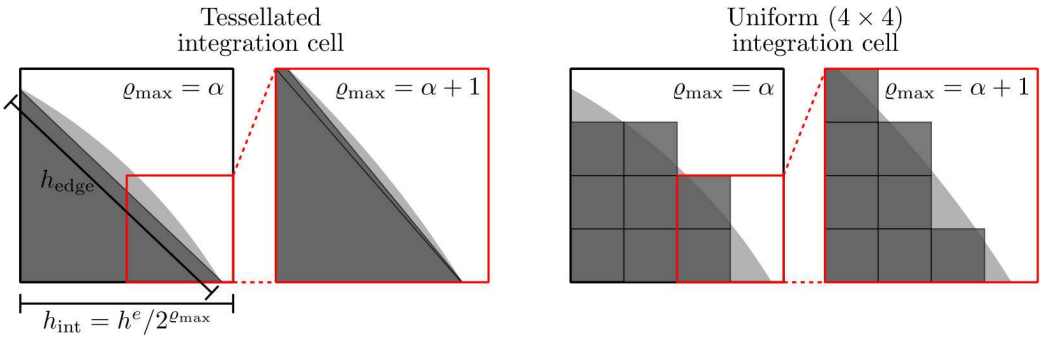

Figure 11: The finest level cells are integrated using either a tessellation-based scheme or a masked uniform (or Gauss) scheme.

not suffer from this problem. The number of uniform integration points used on the finest level does not influence the rate of convergence of the integration error. In fact, using *e.g.* a 4×4 uniform scheme at level $\varrho_{\max} = \alpha$ (see Figure 11) yields exactly the same error as a 2×2 uniform scheme on level $\varrho_{\max} = \alpha + 1$. Since a discontinuous function is integrated over the finest level cells (which is one inside the physical domain and 0 outside), the use of a Gauss integration scheme is counter-intuitive. For the numerical test case in Figure 12a we observe that the Gauss integration scheme is generating reliable results, but that the convergence rate is less stable than that of the uniform scheme.

In Figure 12b we study the dependence of the error magnitude on the radius of curvature of the internal boundary. As indicated above, the integration error per finest level cell is inversely proportional to this radius. Hence, when making the radius R twice as small, the error is increased by a factor of two. This scaling relation is confirmed numerically.

The above analysis and numerical observations pertain to the integration of the unity function over the trimmed domain, but the advantageous convergence properties extend to the case of arbitrary functions.

4.2. Basis function removal strategy

As discussed in Section 3.2 the constructed hierarchical spline spaces are linearly independent by construction. A practical complication, however, is that the trimming of Bézier elements that intersect the boundary of the physical domain will result in basis functions whose support intersects only marginally with this domain. This inevitably leads to poor conditioning of

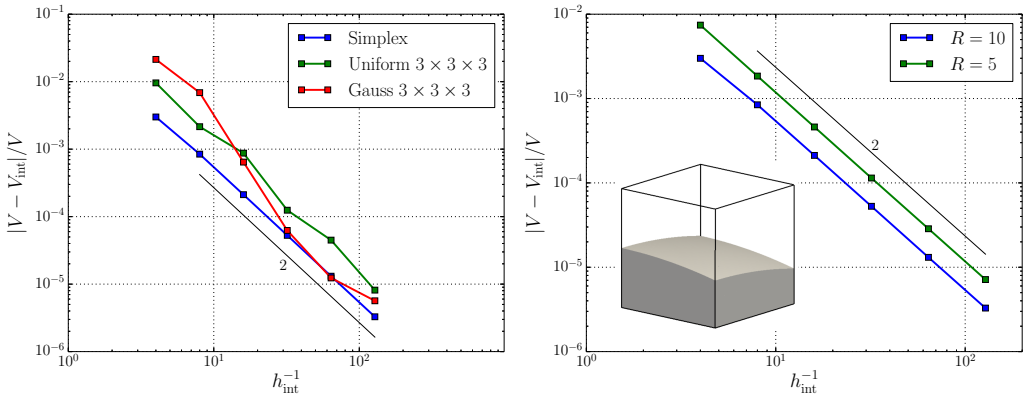

(a) (b)

Figure 12: Convergence of the volume integral of a sphere with radius R intersecting a unit cube while increasing $\varrho_{\max}$ (decreasing h_{int}). (a) Comparison of various integration schemes. (b) Dependence of the simplex-based integration error on the radius of curvature of the sphere.

the linear system of equations, with a negative effect on solver accuracies and iterative solver performance (herein we employ conjugate gradient solvers). A remedy to this problem is to assign a virtual stiffness to the exterior of the trimmed elements, see *e.g.* [8, 9]. Although commonly very small values are used for this virtual stiffness, such an approach in principle nullifies the efforts to construct a smooth approximation of the scan-based geometry. Therefore, we follow the alternative approach to remove basis functions when the volume fraction of their support is smaller than a prescribed tolerance, $0 \leq r_{\text{tol}} \ll 1$, which yields the function space

$$\tilde{\mathcal{H}}_p = \{N_{i,p} \in \mathcal{H}_p \mid r(\text{supp}\,(N_{i,p})) > r_{\text{tol}}\} \subseteq \mathcal{H}_p, \tag{29}$$

with

$$r(\omega) = \left[\frac{\text{vol}\,(\omega \cap \Omega)}{\text{vol}\,(\omega)}\right]^{1/n_d}. \tag{30}$$

The n_d-th root of the volume fraction is used in order to have a consistent interpretation of r_{tol} for the two and three-dimensional cases. When the support of a basis function, $N_{i,p}$, is completely inside the physical domain, $r_i = r(N_{i,p}) = 1$, and it will never be removed. We typically select the tolerance as $r_{\text{tol}} = 2^{-p_{\text{tol}}}$, with the integer power $p_{\text{tol}} > 0$. The rationale is that this allows for the interpretation of r_{tol} in terms of the number of

element bisections as used also for the generation of the trimmed element integration schemes, even though in assessing p_{tol} in relation to $\varrho_{\max}$ (Section 4.1), one must account for the fact that not all basis functions are supported by the same number of elements. We note that a similar basis function removal criterion has been used in *e.g.* [32], with an area-fraction tolerance of $1 \cdot 10^{-6}$.

4.3. Removal of obsolete geometric features

Depending on the selection of the quantity of interest, it can occur that for certain parts of the geometry it is a priori known that they will not contribute to this quantity of interest. More specifically, when effective elastic moduli are to be computed, parts of the geometry that remain unloaded can be removed from the computational domain. Depending on the boundary conditions on such an unloaded part it could undergo rigid body motions, which would make the system of equations ill-posed. Removal of the unloaded parts resolves this ill-posedness issue and is at the same time advantageous from the perspective of computational effort.

The connectivity of the physical domain is determined on the basis of the tessellated integration geometry discussed in Section 4.1. When part of the domain is found to be obsolete, denoted by $\Omega_{\mathrm{obs}} \subset \Omega$, the level set function (2), $f : \Omega \to \mathbb{R}$, is redefined as

$$f_{\mathrm{obs}}(\boldsymbol{x}) = \begin{cases} f(\boldsymbol{x}) & \boldsymbol{x} \notin \Omega_{\mathrm{obs}} \\ \alpha & \text{otherwise} \end{cases}, \tag{31}$$

with α being an arbitrary value smaller than the critical level set value f_{crit}. This redefined level set function yields an implicit representation of the geometry Ω with all obsolete geometric features being removed.

5. Numerical simulations

The isogeometric analysis approach introduced above is studied using three numerical test cases. To study various details of the isogeometric finite cell method, in the first simulation an idealized geometry is considered. Since the exact geometry is known for this test case, the voxel data smoothing scheme is not employed. In the second example, a detailed study of the scan-based adaptive isogeometric approach is conducted for the two-dimensional test case introduced in Section 2. Finally, in the third example the isogeometric

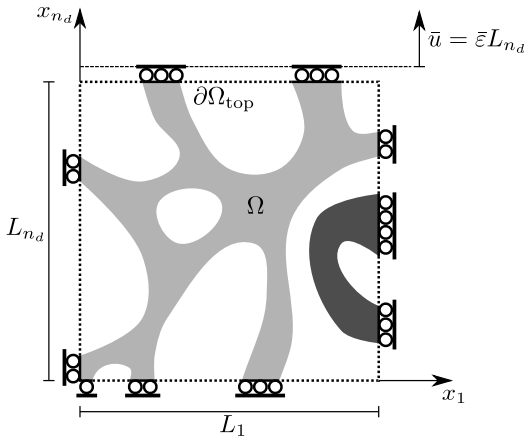

Figure 13: Schematic representation of the computational model set-up. Note that the computational domain Ω consists of two disconnected parts. The rigid body motion of the dark gray part – which is removed from the computational domain – is not constrained by the boundary conditions.

approach is applied to three-dimensional data obtained from a μCT-scan of a trabecular bone micro-structure. The reported number of degrees of freedom pertain in all cases to the vector-valued basis functions of the displacement field $\boldsymbol{u}$.

The set-up of the computational model is for all test cases schematically shown in Figure 13. Note that disconnected parts, such as the dark gray part in Figure 13, are removed from the computational domain, see Section 4.3. The normal displacement is prescribed by $u_n = \boldsymbol{u} \cdot \boldsymbol{n} = \bar{u} = \bar{\varepsilon} L_{n_d}$ on the top boundary $\partial\Omega_{\text{top}} = \{\boldsymbol{x} \in \partial\Omega \mid x_{n_d} = L_{n_d}\}$ and 0 on all other boundaries. Homogeneous Neumann boundary conditions are assumed for the internal boundary $\mathcal{S}$ and the tangential components of the displacement field of $\partial\Omega \backslash \mathcal{S}$. The top boundary displacement is taken equal to $\bar{u} = 0.01 L_{n_d}$ (1 percent tensile straining). For all test cases considered in this contribution these boundary conditions eliminate rigid body motions. Following *e.g.* [21], the Young's modulus is taken as 10 GPa and the Poisson's ratio is assumed to be equal to 0.3.

The quantity of interest is taken as the effective (or apparent) Young's modulus of the specimen, $\mathcal{Q} = \bar{\sigma}/\bar{\varepsilon}$, with the effective strain and stress defined as

$$\bar{\varepsilon} = \frac{\bar{u}}{L_{n_d}} \qquad\qquad \bar{\sigma} = \frac{1}{V_{\text{scan}}} \int_{\Omega} \sigma_{n_d n_d} \, d\boldsymbol{x}, \tag{32}$$

such that

$$\mathcal{Q}(\boldsymbol{u}) = \frac{1}{\bar{\varepsilon} V_{\text{scan}}} \int_{\Omega} \sigma_{n_d n_d} \, d\boldsymbol{x}. \tag{33}$$

The effective stress and strain (32) satisfy the Hill-Mandel energy condition, $\bar{\sigma}\delta\bar{\varepsilon} = V_{\text{scan}}^{-1} \int_{\Omega} \boldsymbol{\sigma} : \delta\boldsymbol{\varepsilon} \, d\boldsymbol{x}$ [33]. Moreover, the effective Young's modulus is independent of the choice of $\bar{u}$ since $\sigma_{n_d n_d}(\boldsymbol{x}) \propto \bar{u}$. For all results presented below the effective Young's modulus is scaled with the elastic modulus E of the bone material: $\bar{E} = \mathcal{Q}/E$.

We note that the computation of the quantity of interest (33) is affected both by the approximation of the solution, $\boldsymbol{u}^h$, and the geometrical error associated with the representation of the computational domain Ω. In the remainder of this section we consider two refinement strategies, one in which the geometry representation is fixed under mesh refinement, and one for which the geometry representation is refined along with the mesh. The latter approach is employed for the computation of the effective modulus of elasticity of the realistic test case. In addition, it is noted that although the quantity of interest (33) is global in the sense that is does not give (local) preference to particular regions in the computational domain, the geometrical complexity of the domain will result in some regions having more influence on the quantity of interest than others. As a result, local refinements that improve the approximation of the quantity of interest are to be expected.

5.1. Two-dimensional idealized geometry

We consider the cross-shaped geometry of Figure 14a. A piecewise analytic level set function is defined to create the arms of the cross and the circular fillets. Note that the fillets can be created exactly by means of a second-order polynomial level set function. Since this idealized geometry is considered within the same framework as used for scan-based geometries, we simulate the complete geometry, although the symmetry of the problem would permit us to only model a quarter of the geometry.

We consider a series of uniform meshes defined with respect to a 2×2 element base mesh. In the following test cases the base mesh is always aligned with the voxel data, but since an analytical level set function is used here, the choice for the base mesh is arbitrary. The various considered meshes consist of $(m_1^0 \cdot 2^{-l_{\text{base}}}) \times (m_2^0 \cdot 2^{-l_{\text{base}}})$, where l_{base} is the number of uniform coarsening steps with respect to the $m_1^0 \times m_2^0$ base mesh. In Figure 14b we show the σ_{22} component of the Cauchy stress obtained on a 16×16 mesh

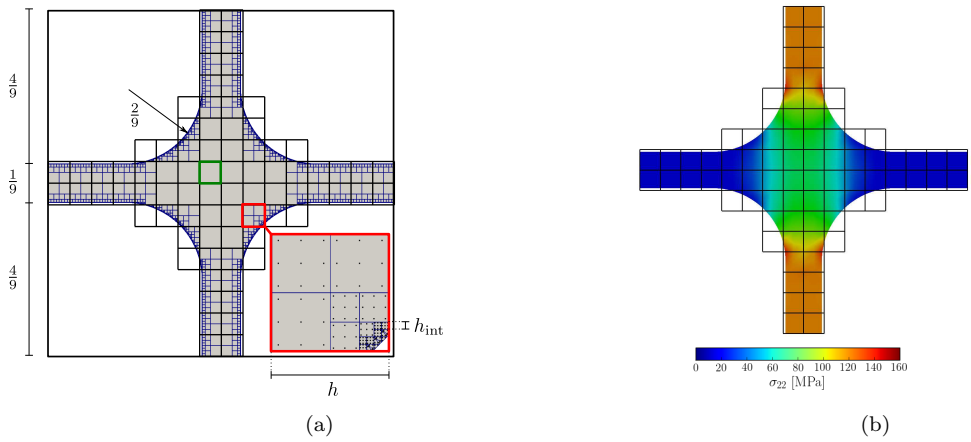

(a) (b)

Figure 14: (a) Geometry and mesh of the idealized geometry. The untrimmed uniform mesh consists of 16×16 elements. After trimming, 20 untrimmed elements (*e.g.* the green element) and 60 trimmed elements (*e.g.* the red element) are present. (b) The σ_{22}-component of the Cauchy stress computed on the mesh shown in (a).

($l_{\text{base}} = -3$) using second-order B-splines. The continuity of the stress field (C^0) is observed from this figure.

All considered meshes consist of regular elements and trimmed elements. In Figure 15 we study the basis function support measure r_i (see Section 4.2) for the various meshes. From Figure 15a it is observed that upon refinement the percentage of basis functions with full support ($r_i = 1$) increases, which is expected since the element volumes scale with $O(h^{n_d})$, while the surface intersections scale with $O(h^{n_d-1})$. The range of the support measure is observed to be very large, in the most extreme case of $l_{\text{base}} = -6$ ranging from $r_{\min} \approx 2^{-7}$ to 2^0. For this case the basis function with the smallest support covers less than $1 \cdot 10^{-4}$ times the volume of the full basis function support. The influence of the basis functions with limited support over the computational domain on the conditioning of the system of equations is shown in Figure 15b. A direct relation is observed between the minimum support measure, $r_{\min}$, and the condition number. It is verified that basis functions with a small support dramatically affect the conditioning of the system.

In Figure 16 we study the influence of the basis function support truncation value, r_{tol}, by ranging its value from 2^{-9} to 2^{-2}. Consistent with the observations in Figure 15b the conditioning of the system can be improved markedly by the removal of basis functions with limited support. Note that for $r_{\text{tol}} \leq 2^{-7}$ no basis functions are removed and hence the condition number

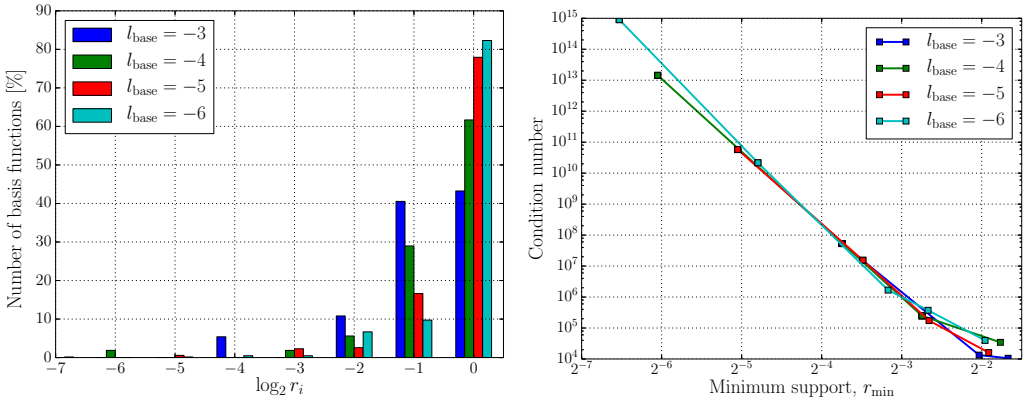

(a) (b)

Figure 15: (a) Distribution of the basis function support measures r_i for the idealized geometry. (b) The relation between the minimal basis function support measure $r_{\min}$ and the condition number of the system of equations. The minumum support value is controlled by gradually increasing the support tolerance r_{tol}.

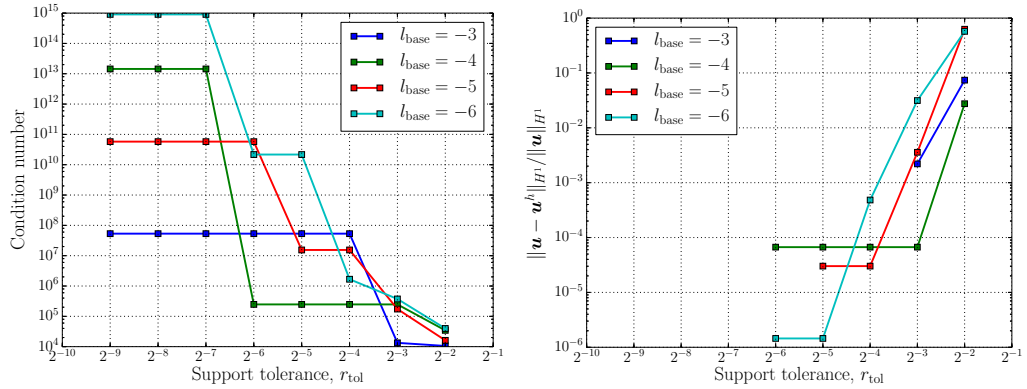

(a) (b)

Figure 16: The influence of the basis function support tolerance r_{tol} on (a) the condition number of the system of equations, and (b) the H^1-error of the solution. Note that since the reference solution $\boldsymbol{u}$ is taken as $\boldsymbol{u}^h$ with $r_{\text{tol}} = 0$, the computed error is zero when no basis functions are removed. Consequently, the corresponding points are not depicted in this error plot.

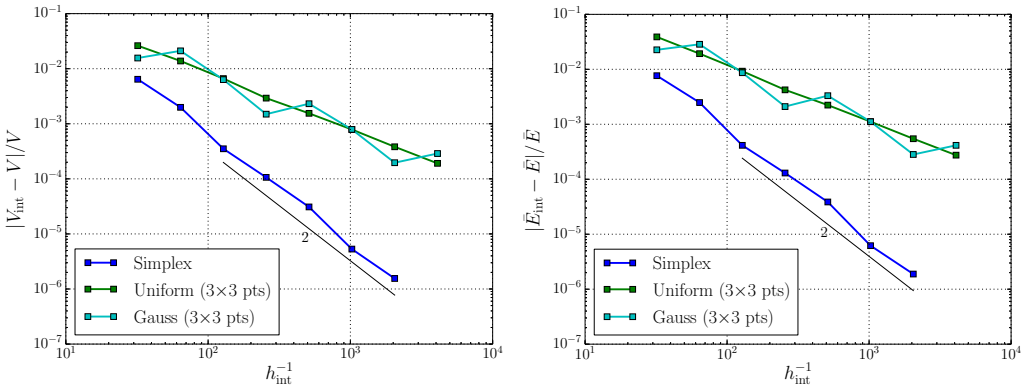

(a) (b)

Figure 17: Effect of the trimmed element integration scheme and integration level on (a) the specimen volume, and (b) the effective Young's modulus.

of the system with all basis functions is reported. For all meshes a dramatic improvement in the conditioning is observed by the removal of only the basis functions with the smallest support, *e.g.* by taking $r_{\text{tol}} = 2^{-6}$ for $l_{\text{base}} = -4$. In Figure 16b the influence of the basis function removal strategy on the H^1-error of the solution is studied, where the reference solution is taken as the discrete solution with $r_{\text{tol}} = 0$ (similar results are obtained for the L^2-error). Removing basis functions clearly affects the accuracy of the solution, but a major loss of accuracy can be circumvented by limiting the value of r_{tol}. It is evident, however, that the selection of r_{tol}, is a delicate task, since choosing it too small results in poor conditioning, while choosing it too large introduces an unwanted source of error. A detailed analysis of the basis function removal criterion – in particular in the context of hierarchical splines – is necessary, but beyond the scope of this paper.

In Figure 17 the influence of the trimmed element integration level, ϱ_{max} (with $h_{\text{int}} = 2^{-\varrho_{\text{max}}} h$), is studied. Second-order splines are considered with $l_{\text{base}} = -3$ (16×16 elements) and $r_{\text{tol}} = 2^{-6}$. It is noted that although the choice of ϱ_{max} influences the accuracy with which the basis function supports r_i are computed, it can be selected independently of the value for r_{tol}. The reason is that all computations are performed on the approximate geometry induced by the element trimming up to the level ϱ_{max}, and that also the basis function removal procedure should pertain to this approximate geometry. An advantage of the simplex scheme is that it always detects contributions on

a smaller scale than the finest level integration cell size, whereas detection of such contributions using uniform or Gaussian schemes depends on the appropriate selection of the number of finest level integration points.

It is observed from Figure 17 that for both the integration of the volume and the effective Young's modulus the predicted second-order convergence rate for the simplex-based integration scheme is recovered, see Section 4.1. In contrast to the results reported in Section 4.1, we now observe a slower rate of convergence (linear) for the uniform and Gaussian integration schemes. This is because for the ideal geometry considered here, the uniform and Gauss schemes consistently overestimate (or consistently underestimate) the exact integral on the straight domain boundaries. The effect that over and underestimating integration cells can partially cancel out is therefore not present here. The first-order convergence rate is in agreement with theoretical expectations. It is stressed that the geometry considered here can be considered as the worst case scenario for the uniform and Gauss integration schemes and that these schemes generally compare more favorably with the simplex-based scheme.

In Figure 18 we show the integration error of the effective modulus of elasticity versus the number of integration points. Since the total number of integration points is governed by the finest level integration cells, the observed second-order convergence rate is expected. When considering the integration error versus the total number of integration points for this test case, the simplex-based scheme compares favorably with the uniform and Gauss schemes. Moreover, it should be noted that the integration error for the simplex-based scheme is purely geometric (*i.e.* over the approximate geometry all functions are integrated exactly), while the error of the other schemes is comprised of both geometric errors and integral approximation errors.

In Figure 19 we study the convergence of the L^2 and H^1-error under uniform mesh refinement. In all results the simplex-based integration scheme is employed. The maximum integration level is taken as $\varrho_{\max} = l_{\text{base}} + 7$, such that the integration geometry is the same for all discretization levels. The reference solution is computed on a mesh which has been refined uniformly several times with respect to the finest mesh shown. The optimal convergence rates of $O(h^{p+1})$ for the L^2-error and $O(h^p)$ for the H^1-error are observed for both linear and quadratic splines. For comparison we also show the convergence behavior for the case that a non-smooth pixel geometry – constructed by only selecting pixels with a volume fraction larger than $\frac{1}{2}$

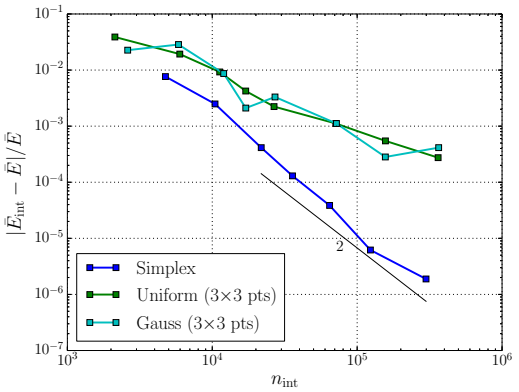

Figure 18: Integration error of the effective Young's modulus versus the number of integration points for various integration schemes.

– is used instead of the smooth geometry. In this case the singularities in the re-entrant corners affect the regularity of the exact solution, which limits the convergence rate. The observed rate of $O(h^{\frac{2}{3}})$ for the H^1-error is in agreement with theoretical expectations [34]. Note that for such non-smooth geometries, there is no benefit in using a higher-order discretization.

In Figure 20a we give the convergence rates of the effective modulus of elasticity under uniform mesh refinement. The rate of $O(h^{2p})$ is in agreement with the expectation. As for the L^2 and the H^1-errors it is observed that the convergence rate improvement for higher-order discretizations is lost when the non-smooth pixel geometry is considered. The effect of the support tolerance, r_{tol}, on the convergence behavior is studied in Figure 20b. For the two values of the support tolerance, the optimal convergence rates are preserved.

5.2. Two-dimensional artificial geometry

We now consider the two-dimensional artificial bone specimen introduced in Section 2. The computational domain is reconstructed from a 32×32 pixel data set. As discussed in Section 4.3 the parts that are disconnected from the top and bottom boundaries have been removed to eliminate unloaded segments. Unless reported otherwise, in the remainder of this section we will use second-order B-splines for both the level set function approximation and the discretization of the primal and dual problems as introduced in Section 3. The focus on second-order splines is motivated by the fact that for this order the benefits of higher-order discretizations are exploited, while the geometry

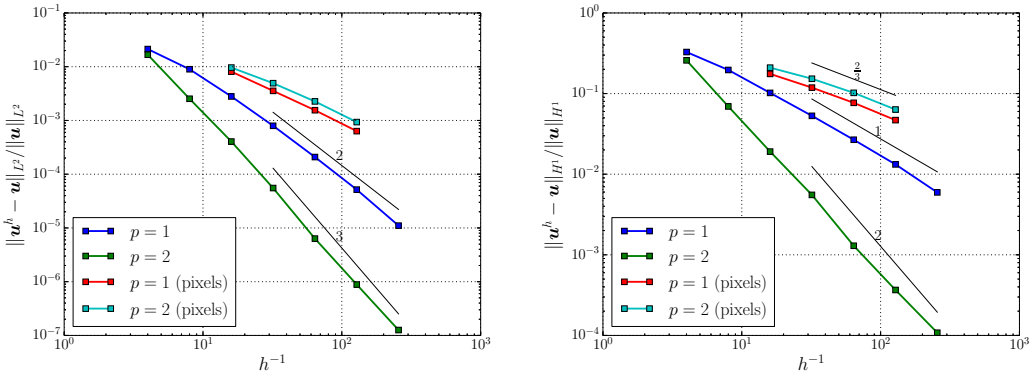

(a) (b)

Figure 19: Convergence behavior of (a) the L^2-error and (b) the H^1-error for the idealized geometry under uniform mesh refinement.

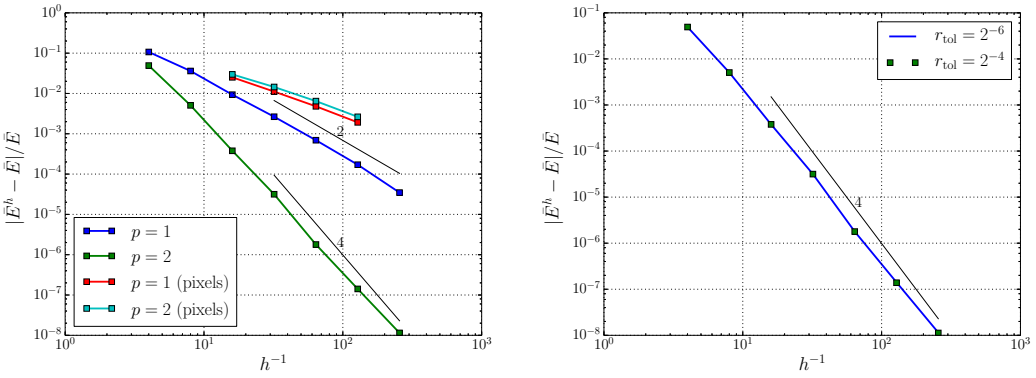

(a) (b)

Figure 20: Convergence of the effective modulus of elasticity for the idealized geometry under uniform mesh refinement.

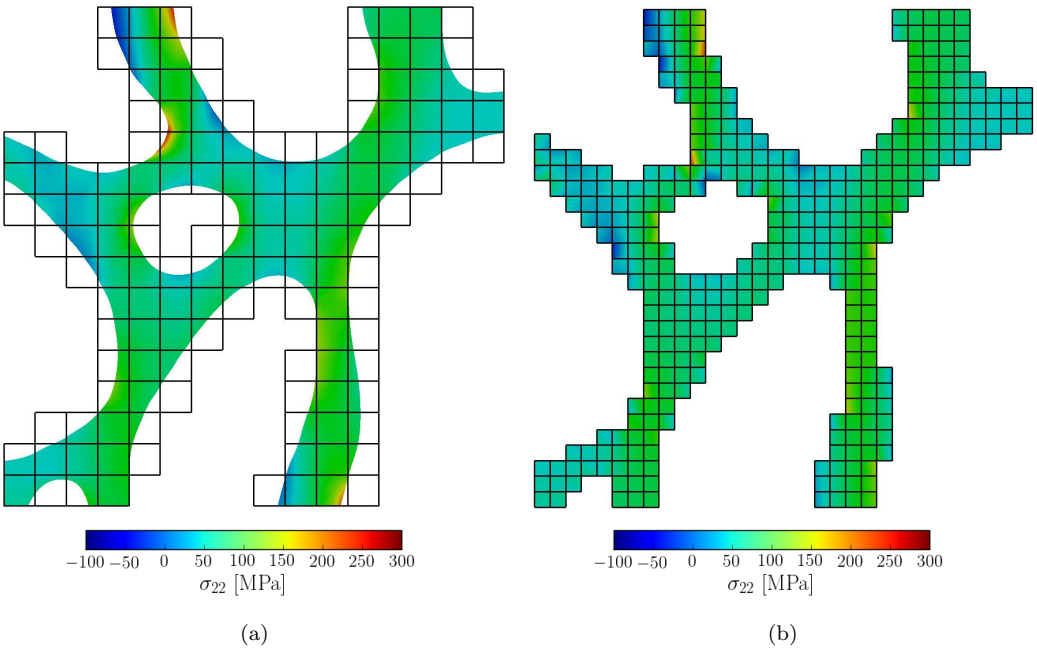

Figure 21: The σ_{22}-component of the Cauchy stress computed (a) on a 16×16 element untrimmed mesh with second-order B-splines, and (b) using the voxel method with the original 32×32 pixels data.

is not smoothed more than necessary (see Section 2.2.3). For all reported results $\varrho_{\max} = 4$ and $r_{\text{tol}} = 2^{-6}$.

In Figure 21a the computed $\sigma_{n_d n_d}$ (with $n_d = 2$) component of the Cauchy stress is computed on a 16×16 element mesh. Compared to the voxel result obtained on the original 32×32 data set, the isogeometric solution obtained on this coarse mesh is capable of representing the expected stress concentrations at re-entrant corners and regions with high curvatures. Compressive stresses due to bending behavior are also accurately represented.

In Figure 22a the convergence of the effective modulus of elasticity under uniform mesh refinement is shown for first and second-order B-splines. Since the level set function for $p = 1$ differs from that for $p = 2$, it is expected that these two orders converge to a (slightly) different value ($\bar{E} = 0.1520$ for $p = 1$ and $\bar{E} = 0.1534$ for $p = 3$). Note that $\varrho_{\max}$ has been chosen sufficiently large to adequately resolve the geometry imposed by the level set function. For comparison also the voxel result ($\bar{E} = 0.1430$) is shown. In contrast to the voxel method, the isogeometric analysis strategy is capable of

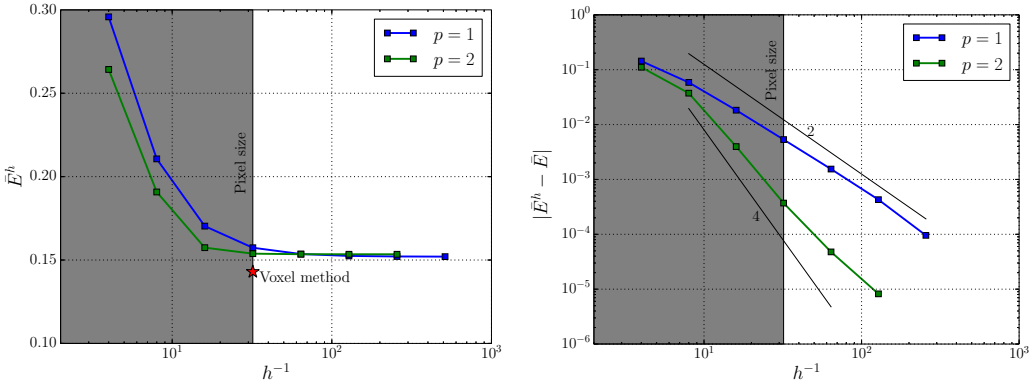

(a) (b)

Figure 22: Convergence of the effective Young's modulus under uniform mesh refinement. The gray area indicates the results for which the computational grid is coarser than the original pixel data ($l_{\text{base}} \geq 0$). The decay of the rate of convergence observed for the second-order spline approximation is attributed to the presence of stress singularities at parts of the domain boundary.

reducing discretization errors under mesh refinement, thereby isolating the geometry approximation error. The ability to control the discretization error is essential for assessing the quality of the computed result. From Figure 22b it is observed that both the first and second-order results converge with rates close to the optimal rates reported in the previous section. The decay in the rate of the second-order results is attributed to the reduced regularity of the exact solution as a consequence of the existence of stress singularities at parts of the domain boundary.

From Figure 23a we observe that the minor loss of the rate of convergence is less visible when the convergence of the quantity of interest is plotted versus the number of degrees of freedom. This is because the exact scaling between the element size and the number of degrees of freedom is lost as a consequence of the removal of unsupported basis functions. Figure 23b shows the effectivity index, $I_{\text{eff}} = \text{Est}/\mathcal{E}$, computed using a dual solution on a (one time) uniformly refined primal mesh. The computed error estimates are of excellent quality for all meshes.

In Figure 24 results are presented obtained using goal-oriented refinements with a refinement fraction of $\eta = 5\%$. Note that since $\varrho_{\max} = 4$ is kept constant under refinement, the trimmed element integration scheme is refined along with the mesh. In the initial step, Figure 24a, the solution is

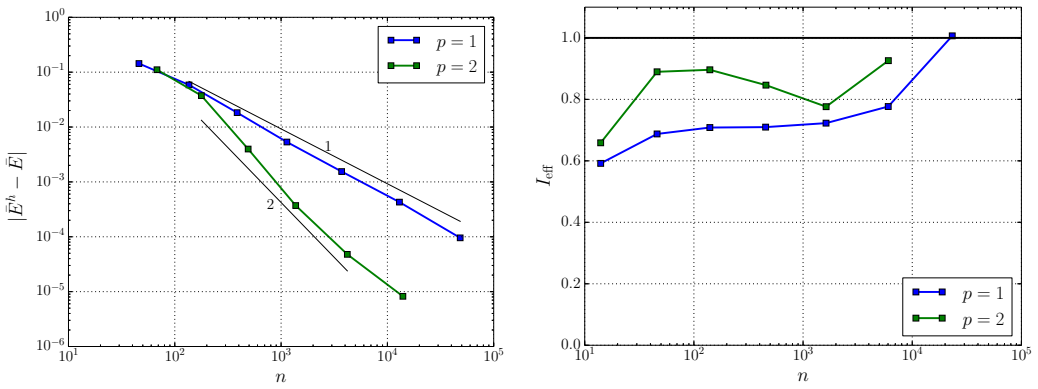

(a) (b)

Figure 23: (a) Convergence of the effective modulus of elasticity versus the total number of degrees of freedom for various uniformly refined meshes. (b) The effectivity indices have been computed using a dual solution on a (one time) uniformly refined primal mesh.

computed on a 4×4 untrimmed initial mesh, which evidently is too coarse to resolve the stress field – and in particular the stress concentrations – accurately. From the dual solution and the dual-weighted residual density for this step, Figure 25a and 25b, it is observed that there are multiple regions to be refined, which, as a consequence of the support tagging strategy discussed in Section 3.3, will result in an almost global refinement. At the second step of refinement, Figures 25c and 25d, the dual solution is well resolved and the dual-weighted residual density indicates a preference for refinement around the high curvature boundaries in the top-left region of the domain. From Figure 24b it is observed that refinements are indeed confined to that region, and that the main features of the stress field are well resolved with only 69 elements and 232 vector-valued shape functions. As observed from Figures 25e and 25f, further refinements are directed toward the region surrounding the cavity in the specimen, leading to the mesh in Figure 24c. At further stages of refinement, the stress concentrations at the re-entrant boundary corners are resolved, see Figure 24d.

In Figure 26a we show the convergence of the quantity of interest under adaptive refinement for various refinement fractions, η. It is observed that the optimal rates are accurately recovered using all refinement fractions. Comparison with the convergence behavior under uniform refinement, Figure 23a, shows that under adaptive refinement the optimal rate is recovered regardless of the stress singularities in the boundary corners. This is a

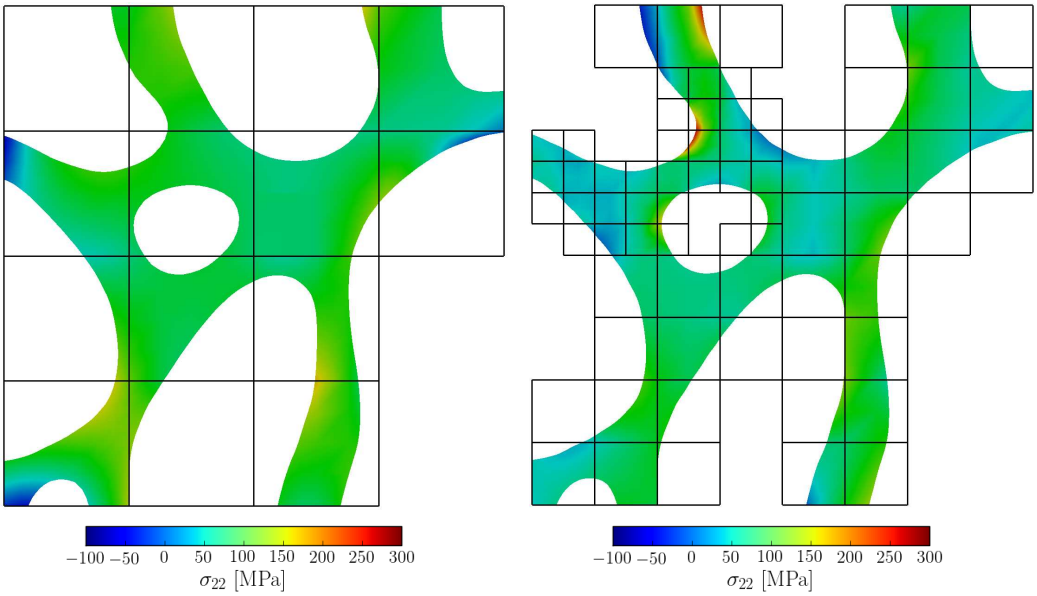

(a) Step 1: $m = 14$, $n = 68$

(b) Step 3: $m = 69$, $n = 232$

(c) Step 6: $m = 224$, $n = 668$

(d) Step 11: $m = 1852$, $n = 4426$

Figure 24: Goal-oriented adaptive refinement of the artificial bone specimen with refinement fraction $\eta = 5\%$.

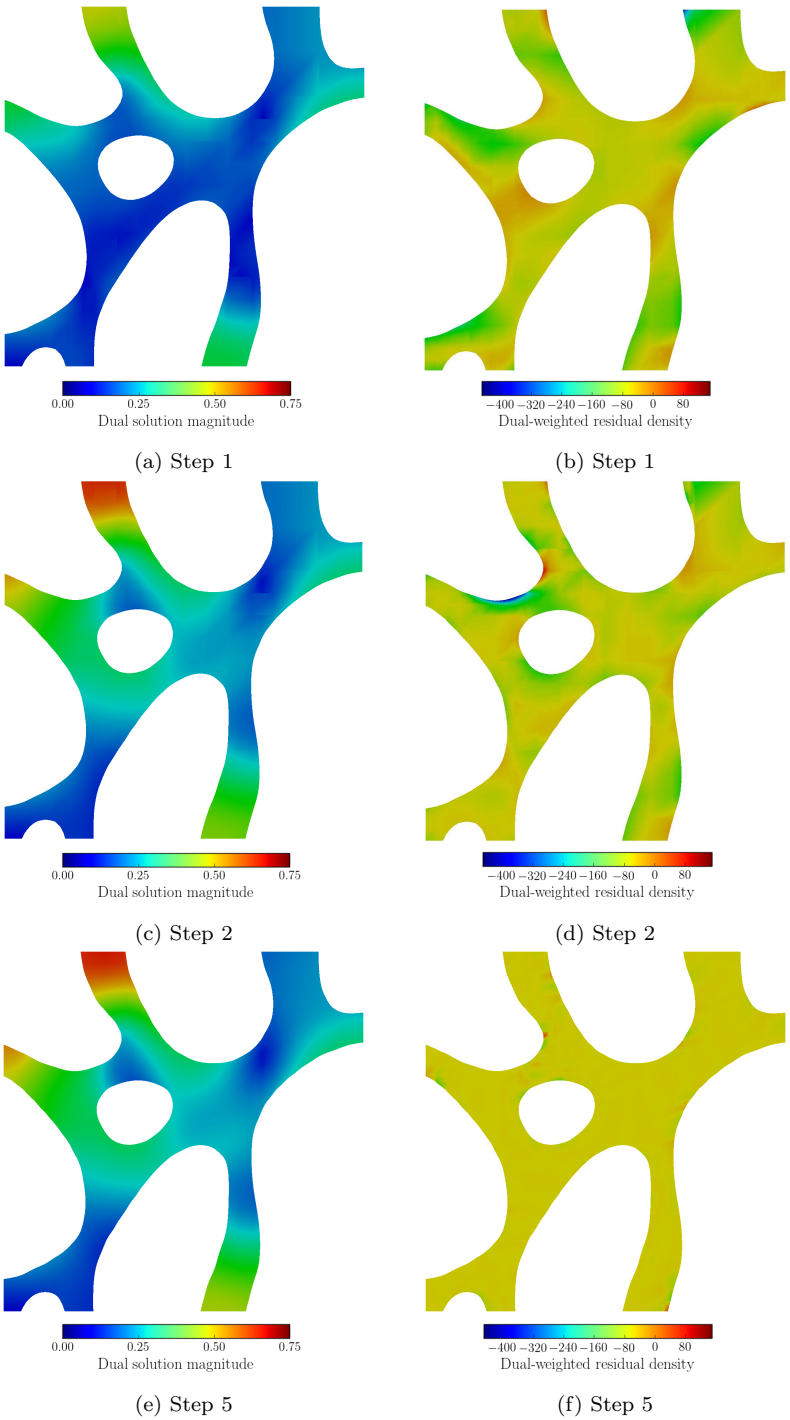

(a) Step 1 (b) Step 1

(c) Step 2 (d) Step 2

(e) Step 5 (f) Step 5

Figure 25: Dual solution and dual-weighted residual density computed at three adaptive refinement steps with refinement fraction $\eta = 5\%$.

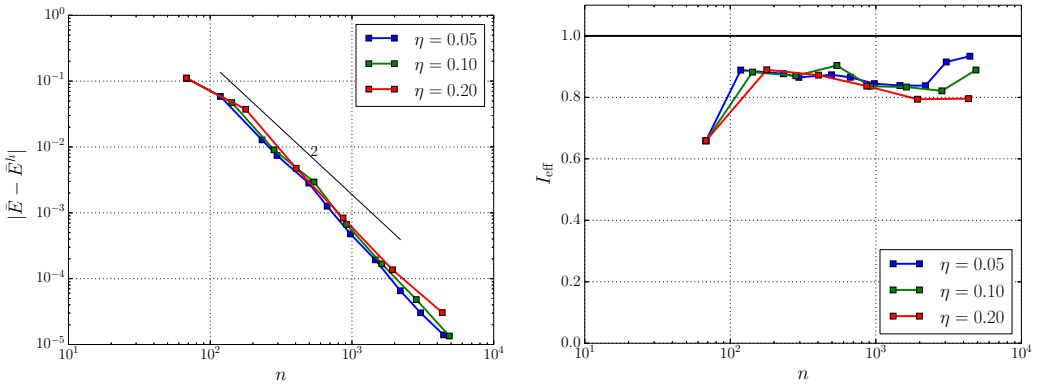

(a) (b)

Figure 26: (a) Convergence of the quantity of interest (effective Young's modulus) for the artificial bone specimen under adaptive refinement with various refinement fractions. (b) Effectivity index of the error estimate under adaptive refinement.

consequence of the ability of the refinement procedure to localize refinements to the regions of influence of these singularities, see Figure 24d. Closer inspection reveals that the errors obtained using a small refinement fraction are smaller than those with larger fractions. This is a consequence of the local refinements being better tailored to the intermediate solutions. In Figure 26b the effectivity index is shown under adaptive refinement. The computed estimates under adaptive refinement are of an even better quality than those for uniform refinements (Figure 23b).

5.3. Patient-specific geometry

In the final example we compute the effective modulus of elasticity of a scanned trabecular bone specimen. The gray scale data that serve as input to the computation is obtained from a μCT-scan of a femur, see Figure 27a. The analyzed data contains $32 \times 32 \times 32$ voxels, with the voxel size equal to 40 μm (the domain size $L_d = 1.28\,\text{mm}$). In Figure 27b we show the smooth geometry extracted from the voxel data. For all results reported in this section second-order B-splines have been used, $\varrho_{\max} = 3$ and $r_{\text{tol}} = 2^{-6}$. The parts of the geometry that remain unloaded, which are marked in dark gray in Figure 27b, have been removed from the computational domain.

In Figure 28 three adaptive refinement steps are shown for the refinement fraction $\eta = 2.5\%$, and two details of the solution are shown in Figures 29 and 30. From Figure 29a it is observed that stress concentrations are present

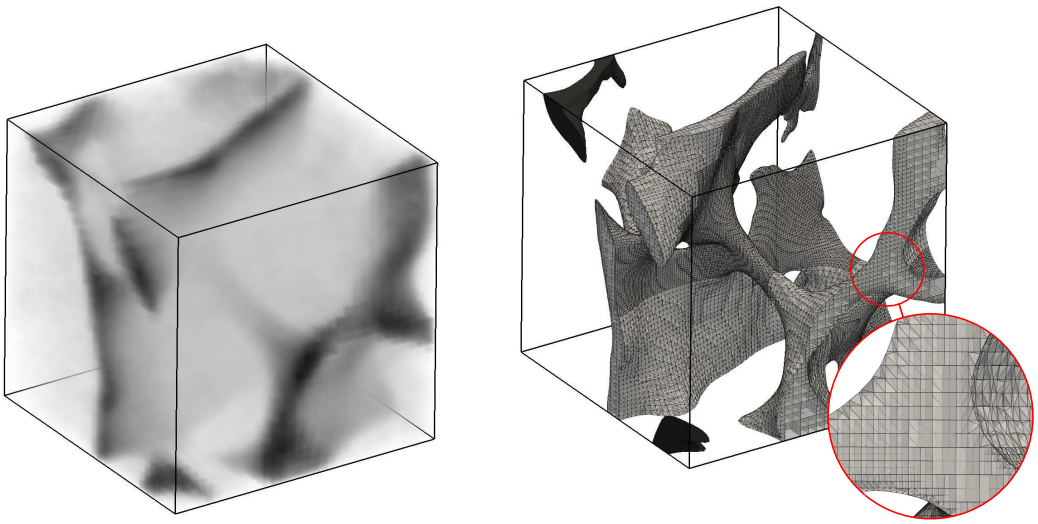

(a) (b)

Figure 27: (a) Volume plot of the $32 \times 32 \times 32$ voxels gray scale data (the opacity is scaled with the gray scale). (b) The trimmed mesh extracted from the second-order B-spline level set approximation of the voxel data shown in (a).

in the $8 \times 8 \times 8$ initial mesh on parts that are supposed to be unloaded. This is because although the geometry shown in the detail is disconnected, the support of a coarse basis function covers both sides of the observed gap. As a consequence, from the discretization perspective the two parts are connected, which results in unphysical stresses. The adaptive refinement scheme is capable of detecting this type of undesirable behavior by locally refining the mesh in the vicinity of the shown detail. In Figure 29b it is observed that already after two refinement steps the mesh is sufficiently refined to eliminate the unphysical stresses. Once these unphysical stresses have been removed, the shown detail becomes of minor importance to the quantity of interest, and further refinement in this region is limited in the subsequent steps, see Figure 29c.

From both details it is observed that since $\varrho_{\max}$ is defined with respect to the element size, the integration geometry is refined along with the mesh. This geometry refinement is required to accurately represent important features of the solution, such as stress concentrations around cavities, see Figure 30.

In Figure 31 the convergence of the error estimate under adaptive re-

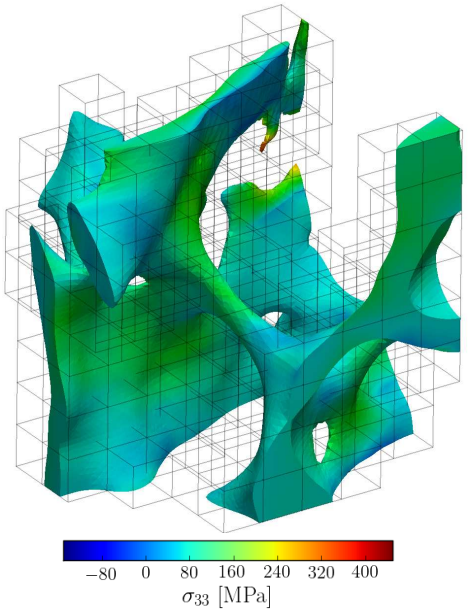

(a) Step 1: $m = 225$, $n = 2325$

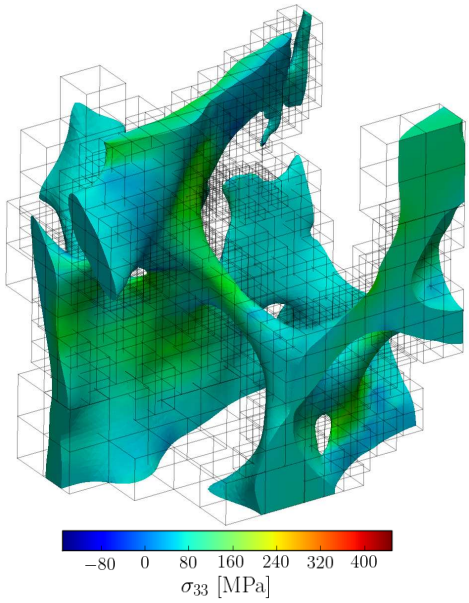

(b) Step 3: $m = 1110$, $n = 7800$

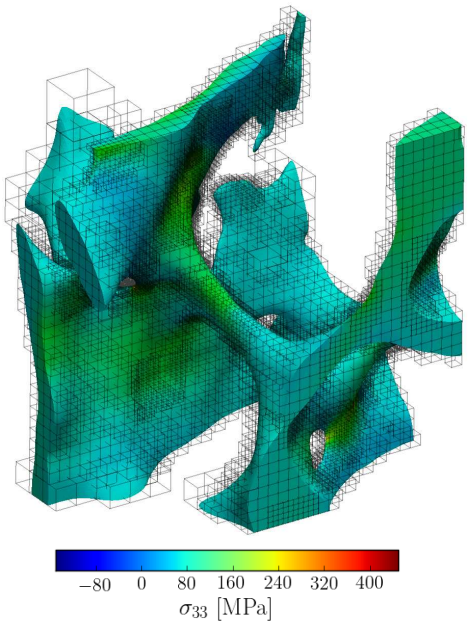

(c) Step 7: $m = 14670$, $n = 61224$

Figure 28: Goal-oriented adaptive refinement of the $32 \times 32 \times 32$ voxel data scan-based geometry with refinement fraction $\eta = 2.5\%$.

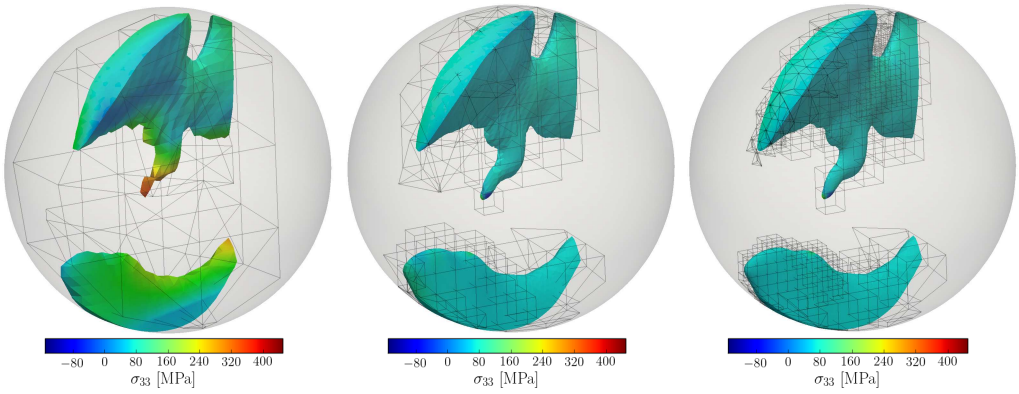

(a) Step 1 (b) Step 3 (c) Step 7

Figure 29: Detail of the patient-specific geometry computation shown in Figure 28 at three refinement steps.

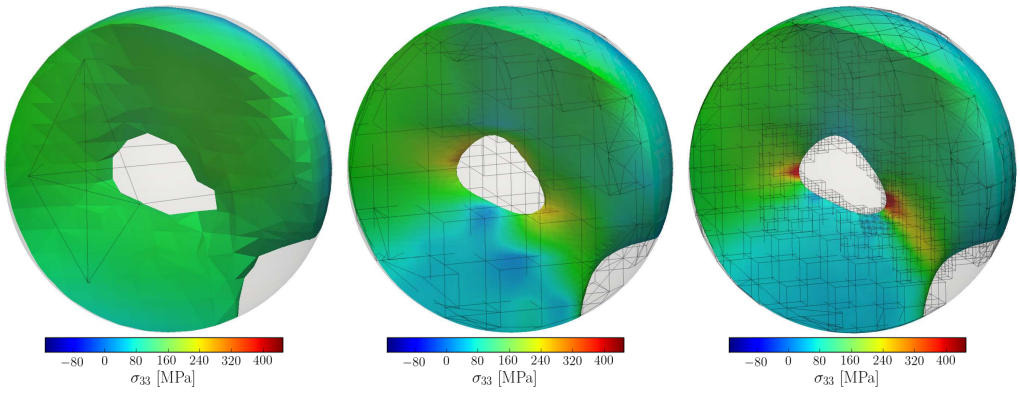

(a) Step 1 (b) Step 3 (c) Step 7

Figure 30: Detail of the patient-specific geometry computation shown in Figure 28 at three refinement steps.

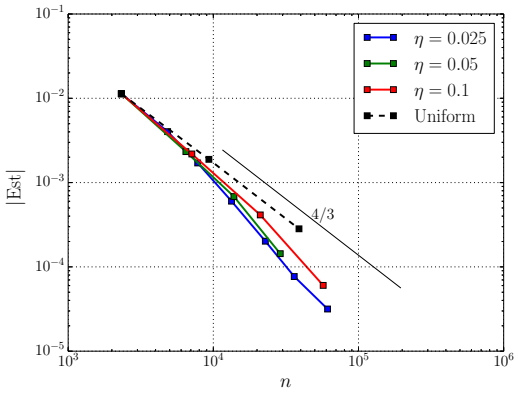

Figure 31: Convergence of the estimator of the quantity of interest (effective Young's modulus) for the patient-specific geometry with various refinement fractions.

finement is shown for various refinement fractions. Despite the fact that a high accuracy reference solution cannot be obtained for this test case, the error estimate gives insight into the accuracy of the computed solutions. For example, using the adaptive results with refinement fraction $\eta = 2.5\%$ the effective modulus of elasticity is computed as $\bar{E}^h = 0.0216$ with the error estimator $\text{Est} = -3.16 \cdot 10^{-5}$ (the minus sign indicates that the computed effective modulus of elasticity is an overestimate). The fact that the error estimates converge at the optimal rates adds confidence to their reliability. From Figure 31 it is also observed that the adaptive strategy performs considerably better in terms of accuracy in relation to the number of degrees of freedom than uniform refinements. As with the artificial specimen studied in the previous section, for a fixed number of degrees of freedom a small refinement fraction yields a more accurate result than a larger refinement fraction.

6. Conclusions

We have proposed a computational methodology for the determination of the effective elastic properties of structures represented by voxel scan data. This methodology consists of two main steps. In the first step, a B-spline-based approximation is used to obtain a smooth level set function. This level set function provides an implicit definition of the physical domain – which is generally of high geometric and topological complexity – with a smooth boundary within the scan volume. In this contribution we used

a level set function only for the definition of the geometry, but a similar approach could be used to smoothen scan-based material property data. In the second step the isogeometric finite cell method is used in combination with a goal-adaptive refinement strategy to efficiently compute the quantity of interest.

Our analysis of the level set approximation of the voxel data reveals that the proposed smoothing strategy behaves approximately as a Gaussian filter. An important consequence is that high-frequency features (relative to the voxel size) are filtered out. This property is particularly advantageous when the primary geometric features of the specimen (*e.g.* the trabeculae) are represented by a relatively small number of voxels. In that case, the physically unrealistic non-smoothness of the voxel data is removed, while a sensible geometry in recovered. A potentially undesirable side effect of the smoothing procedure is that sharp geometric features that are just resolved by the scan resolution are subject to unrealistic smoothing. To avoid unnecessary loss of geometric information we have limited the used spline order to $p = 2$ for the test cases considered in this contribution. For arbitrary scan data the choice of spline order will depend on the amount of smoothing that is desired by the analyst.

An essential aspect of the proposed analysis strategy is the integration of trimmed elements, *i.e.* the elements that intersect the boundary of the physical domain. We have used a multi-level integration scheme with a simplex tessellation on the finest scale of bisection. In the context of adaptive analysis it is an advantage of this simplex-based integration scheme that it converges asymptotically under mesh refinement. The multi-level integration schemes generally generate a large number of integration points over the trimmed elements, which leads to computationally expensive assembly routines. We have partially ameliorated this drawback by evaluating the integrals in parallel. The usage of an integration point lumping scheme [35] could be advantageous, although the effect of such a scheme on the optimality of the obtained results has to be assessed. A final advantage of the simplex-based integration scheme is that a boundary parametrization is obtained from the tessellation procedure. Although this parametrization is not used in this work, its availability would permit for the evaluation of surface integrals, thereby facilitating the imposition of non-homogeneous Neumann boundary conditions or weakly-imposed Dirichlet boundary conditions.

We have found that the isogeometric finite cell method converges with the theoretically expected rates for all considered test cases. Optimal con-

vergence rates are found for the computation of the effective Young's modulus using a goal-adaptive analysis with a range of refinement fractions. A detailed visual inspection of the computational results for a trabecular bone micro-structure has shown that the goal-adaptive strategy is capable of realistically representing various distinctive features of the solution.

An essential aspect is the removal of basis functions with a small support over the physical domain. Since we have used iterative solvers for all test cases, improving the conditioning of the system of equations by removing basis functions significantly reduces the solving time. Although we obtained accurate results using iterative solvers, as also indicated in [13], the development of efficient iterative solvers and pre-conditioners should be an important aspect of future research in the context of finite cell methods. The selection of the basis function support tolerance is another topic of further study. For the test cases we have been able to select the truncation value such that a good balance is obtained between system conditioning and computational accuracy, but a more systematic approach is needed.

Acknowledgement

The research of C.V. Verhoosel was funded by the Netherlands Organization for Scientific Research (NWO) under the VENI scheme.

Bibliography

[1] T. J. R. Hughes, J. A. Cottrell, Y. Bazilevs, Isogeometric analysis: CAD, finite elements, NURBS, exact geometry and mesh refinement, Computer Methods in Applied Mechanics and Engineering 194 (39-41) (2005) 4135–4195.

[2] J. A. Cottrell, T. J. R. Hughes, Y. Bazilevs, Isogeometric Analysis: Toward Integration of CAD and FEA, Wiley, Chichester, 2009.

[3] F. Auricchio, L. B. Da Veiga, T. J. R. Hughes, A. Reali, G. Sangalli, Isogeometric collocation methods, Mathematical Models and Methods in Applied Sciences 20 (11) (2010) 2075–2107.

[4] D. Schillinger, J. A. Evans, A. Reali, M. A. Scott, T. J. R. Hughes, Isogeometric collocation: Cost comparison with Galerkin methods and extension to adaptive hierarchical NURBS discretizations, Computer Methods in Applied Mechanics and Engineering 267 (2013) 170–232.

[5] M. J. Borden, M. A. Scott, J. A. Evans, T. J. R. Hughes, Isogeometric finite element data structures based on Bézier extraction of NURBS, International Journal for Numerical Methods in Engineering 87 (1–5) (2011) 15–47.

[6] M. A. Scott, M. J. Borden, C. V. Verhoosel, T. W. Sederberg, T. J. R. Hughes, Isogeometric finite element data structures based on Bézier extraction of T-splines, International Journal for Numerical Methods in Engineering 88 (2) (2011) 126–156. doi:10.1002/nme.3167.

[7] F. Irzal, J. J. C. Remmers, C. V. Verhoosel, R. De Borst, An isogeometric analysis Bézier interface element for mechanical and poromechanical fracture problems, International Journal for Numerical Methods in Engineering 97 (8) (2014) 608–628. doi:10.1002/nme.4615.

[8] E. Rank, M. Ruess, S. Kollmannsberger, D. Schillinger, A. Düster, Geometric modeling, isogeometric analysis and the finite cell method, Computer Methods in Applied Mechanics and Engineering 249–252 (2012) 104–115.

[9] D. Schillinger, L. Dede, M. A. Scott, J. A. Evans, M. J. Borden, E. Rank, T. J. R. Hughes, An isogeometric design-through-analysis methodology based on adaptive hierarchical refinement of NURBS, immersed boundary methods, and T-spline CAD surfaces, Computer Methods in Applied Mechanics and Engineering 249–252 (2012) 116–150.

[10] J. Parvizian, A. Düster, E. Rank, Finite cell method, Computational Mechanics 41 (1) (2007) 121–133.

[11] A. Düster, J. Parvizian, Z. Yang, E. Rank, The finite cell method for three-dimensional problems of solid mechanics, Computer Methods in Applied Mechanics and Engineering 197 (45) (2008) 3768–3782.

[12] A. V. Vuong, C. Giannelli, B. Jüttler, B. Simeon, A hierarchical approach to adaptive local refinement in isogeometric analysis, Computer Methods in Applied Mechanics and Engineering 200 (49–52) (2011) 3554–3567.

[13] D. Schillinger, M. Ruess, The finite cell method: A review in the context of higher-order structural analysis of CAD and image-based geometric models, Archives of Computational Methods in Engineering (2014) 1–65.

[14] A. Düster, H.-G. Sehlhorst, E. Rank, Numerical homogenization of heterogeneous and cellular materials utilizing the finite cell method, Computational Mechanics 50 (4) (2012) 413–431.

[15] M. Ruess, D. Tal, N. Trabelsi, Z. Yosibash, E. Rank, The finite cell method for bone simulations: verification and validation, Biomechanics and Modeling in Mechanobiology 11 (2012) 425–437.

[16] S. J. Hollister, J. M. Brennan, N. Kikuchi, A homogenization sampling procedure for calculating trabecular bone effective stiffness and tissue level stress., Journal of Biomechanics 27 (4) (1994) 433–444.

[17] B. van Rietbergen, H. Weinans, R. Huiskes, A. Odgaard, A new method to determine trabecular bone elastic properties and loading using micromechanical finite-element models, Journal of Biomechanics 28 (1) (1995) 69–81.

[18] B. van Rietbergen, H. Weinans, R. Huiskes, B. J. W. Polman, Computational strategies for iterative solutions of large fem applications employing voxel data, International Journal for Numerical Methods in Engineering 39 (16) (1996) 2743–2767.

[19] P. Frey, B. Sarter, M. Gautherie, Fully automatic mesh generation for 3-D domains based upon voxel sets, International Journal for Numerical Methods in Engineering 37 (16) (1994) 2735–2754.

[20] R. Müller, P. Rüegsegger, Three-dimensional finite element modelling of non-invasively assessed trabecular bone structures, Medical Engineering & Physics 17 (2) (1995) 126–133.

[21] D. Ulrich, B. van Rietbergen, H. Weinans, P. Rüegsegger, Finite element analysis of trabecular bone structure: a comparison of image-based meshing techniques, Journal of Biomechanics 31 (12) (1998) 1187–1192.

[22] M. Ainsworth, J. T. Oden, A posteriori error estimation in finite element analysis, Wiley, 2000.

[23] G. Kuru, C. V. Verhoosel, K. G. van der Zee, E. H. van Brummelen, Goal-adaptive isogeometric analysis with hierarchical splines, Computer Methods in Applied Mechanics and Engineering 270 (2014) 270–292. doi:10.1016/j.cma.2013.11.026.

[24] L. C. Evans, Partial Differential Equations, The American Mathematical Society, 2010.

[25] M. G. Cox, The numerical evaluation of B-splines, IMA Journal of Applied Mathematics 10 (2) (1972) 134–149.

[26] C. de Boor, On calculating with B-splines, Journal of Approximation Theory 6 (1) (1972) 50–62.

[27] M. Unser, A. Aldroubi, M. Eden, On the asymptotic convergence of B-spline wavelets to Gabor functions, Information Theory, IEEE Transactions on 38 (2) (1992) 864–872.

[28] M. Abramowitz, I. A. Stegun, Handbook of Mathematical Functions, Dover Publications, New York, 1964.

[29] T. M. Lehmann, C. Gonner, K. Spitzer, Survey: Interpolation methods in medical image processing, Medical Imaging, IEEE Transactions on 18 (11) (1999) 1049–1075.

[30] L. G. Shapiro, G. C. Stockman, Computer Vision, Prentice Hall, 2001.

[31] L. Dedè, H. A. F. A. Santos, B-spline goal-oriented error estimators for geometrically nonlinear rods, Computational Mechanics 49 (1) (2012) 35–52.

[32] A. Embar, J. Dolbow, I. Harari, Imposing Dirichlet boundary conditions with Nitsche's method and spline-based finite elements, International Journal for Numerical Methods in Engineering 83 (2010) 877–898.

[33] R. Hill, Elastic properties of reinforced solids: some theoretical principles, Journal of the Mechanics and Physics of Solids 11 (5) (1963) 357–372.

[34] C. Johnson, Numerical solution of partial differential equations by the finite element method, Dover Publications, 2012.

[35] Z. Yang, M. Ruess, S. Kollmannsberger, A. Düster, E. Rank, An efficient integration technique for the voxel-based finite cell method, International Journal for Numerical Methods in Engineering 91 (5) (2012) 457–471.